Modulation of kinase activity within a bacterial membraneless organelle

Saumya Saurabh [1], Trisha N. Chong [1], Camille Bayas [2†], Peter D. Dahlberg [2], Heather N. Cartwright [3‡], W. E. Moerner [2], and Lucy Shapiro [1*]

[1]Department of Developmental Biology, Stanford University School of Medicine, Stanford, CA, USA

[2] Department of Chemistry, Stanford University, Stanford, CA, USA

[3] Department of Plant Biology, Carnegie Institution for Science, Stanford, CA, USA

***** Corresponding author

Present address:

† Machine Learning and Imaging, Indigo Ag., 500 Rutherford Ave, Boston, MA, USA

‡ Intelligent Imaging Innovations (3i), 3575 Ringsby Court, Suite 102, Denver, CO, USA

Abstract

Maintenance of robust biochemical signaling is essential for oligotrophic bacteria that survive under fluctuating environmental challenges. We report that a polar membraneless organelle in *Caulobacter crescentus* forms by phase separation and tunes a critical phospho-signaling pathway to nutrient availability using the hydrotrope effect of ATP. Sequestration of the signaling pathway within this specialized polar microdomain utilizes the phase transition parameters of a disordered protein to regulate the activity of a localized kinase. Under low ATP concentrations, phase separation in the microdomain is reinforced, enhancing kinase activity, and thereby conferring control of a critical cell cycle signaling pathway to the physical properties of the membraneless organelle.

Main text

Membraneless organelles serve diverse functions such as compartmentalization of biomolecules, regulation of biochemical reactions, and response to stress *(1, 2)* . In eukaryotic cells, reversible sequestration of regulatory molecules into condensates is an emergent stress-response mechanism often achieved by a complex interplay between the membrane-confined nucleus and membraneless compartments *(3, 4)*. Unlike eukaryotic cells, bacteria lacking membrane-bound compartments have evolved to robustly regulate signaling, especially under exposure to environmental assaults *(5)*. How free-living bacteria translate ever-changing environmental cues into signaling reactions that drive their cell cycle and proliferation, is a critical but unanswered question. We now know that single cell bacteria utilize membraneless organelles for organizing biomolecules *(6-10)*. The composition and function of membraneless organelles are often attributed to their physical properties *(1, 11)*. Membraneless organelles may be formed via liquid-liquid phase separation and are known to be affected by several environmentally regulated factors such as salt concentration, pH, crowding and temperature *(12)*. Therefore, membraneless organelles in oligotrophic bacteria that survive under dilute nutrient conditions in the wild are potential model systems to determine how phase transitions regulate signaling pathways in response to environmental cues.

Asymmetric cell division is a fundamental process that requires exquisite spatio-temporal organization of signaling pathways *(10, 13)*. *Caulobacter crescentus* (hereafter, *Caulobacter*) is a Gram-negative, oligotrophic bacterium that divides asymmetrically yielding a sessile stalked cell and a motile swarmer cell during each cell cycle (Fig. 1A). The sequestration of a signaling pathway within a membraneless organelle at the flagellar pole of the pre-divisional cell enables asymmetric cell division yielding daughter cells with different cell fates (Fig. 1A) *(10)*. The swarmer cell is incapable of DNA replication and cell division until it differentiates into a stalked cell. A hallmark of differentiation of a swarmer cell into a stalked cell is a change in the protein composition of the polar microdomain at the flagellated cell pole that comprises the pole organizing protein PopZ *(10, 14)* (Fig. 1A). Differentiation is also marked by the loss of flagellum and initiation of stalk biogenesis. Coincident with stalk biogenesis, a newly expressed protein, SpmX, localizes to the stalk-bearing pole through a direct interaction with PopZ in the cytoplasm

(15, 16). SpmX is a trans-membrane protein that subsequently localizes the trans-membrane histidine kinase DivJ to the stalk-bearing cell pole *(15, 16)*. Time lapse microscopy of single *Caulobacter* cells harboring fluorescently-tagged PopZ, SpmX and DivJ revealed the sequential appearance of these proteins at the cell pole (Fig. 1B). High-resolution imaging of PopZ and SpmX *in situ* suggests that SpmX localizes to the inner membrane and extends into the cytoplasm at one side of the pole, while PopZ forms a cytoplasmic space-filling dome at the cell pole (Fig. 1C) *(17, 18)*. Previous biochemical measurements have shown that SpmX interacts directly with both PopZ and DivJ, while PopZ and DivJ do not interact *(16)*. Together, biochemical and imaging data suggest that SpmX and DivJ likely form a membrane-associated complex, where SpmX serves as an adapter to localize DivJ to a specific region of the PopZ microdomain (Fig. 1C). The mechanism behind the formation of this polar organelle, and its role in regulating DivJ kinase activity are unknown.

DivJ's polar localization and its ability to catalyze its own phosphorylation are intimately tied to the *Caulobacter* stalked cell development program through a sustained phosphorelay *(15, 19, 20)*. Once the swarmer cell differentiates into a stalked cell, SpmX and DivJ remain stably localized to the stalk-bearing pole for all subsequent cell cycles. Accordingly, we asked if SpmX plays a regulatory role in DivJ's stable localization and kinase activity. Both PopZ and SpmX have predicted Intrinsically Disordered Regions (IDRs) rich in prolines and negatively charged amino acids (Fig. 1D). A subset of proteins containing IDRs have been shown to form biomolecular condensates via phase separation both *in vitro* and *in vivo (21)*. To test whether PopZ and SpmX can phase separate *in vitro*, we purified and labelled these proteins with fluorescent dyes (Supplementary text). Microscopic observation of fluorescently-tagged proteins in solution showed that while DivJ(ΔTM) remained soluble under physiological salt concentration and pH, both PopZ and SpmX(ΔTM) formed spherical condensates under the same conditions (Fig. 1E and S1). Purified IDRs from SpmX (aa 156-355) and PopZ (aa 1-102) were necessary and sufficient for phase separation *in vitro* (Fig. 1F). Condensate formation was promoted by crowding (Fig. S2A) and could be reversed by addition of salt at high concentrations (Fig. S2B, SI videos 1 and 2), underscoring the role of charged residues in the IDRs in PopZ and SpmX phase separation. The structured

domains of SpmX (aa 1-155) and PopZ (aa 103-177) did not form condensates at the concentrations tested (Fig. 1F). However, these domains contributed to stronger self-interaction within the condensates, as measured by fluorescence recovery after photobleaching (FRAP) *in vitro* (Fig. S3). Together, in-solution experiments with purified PopZ suggest that PopZ exists as a condensate in the cell, formed by phase separation. However, these experiments ignore the physiological, two-dimensional topology of SpmX.

To test whether SpmX phase separates in its correct membrane bound topology, we reconstituted SpmX *in vitro* on supported lipid bilayers (SLBs) *(22)* and *in vivo* in *E. coli*. Briefly, poly-histidine tagged SpmX(ΔTM) was attached to a lipid bilayer composed of 0.1% (by weight) Nickel-chelated phospholipids (Supplementary text). Microscopic observation of lipid bilayers revealed fluorescent puncta (Fig. S4A) that could be dissolved by adding salt at high concentrations (Fig. S4B, SI video 5), implying that these puncta were SpmX condensates as opposed to irreversible aggregates. Additionally, SpmX and PopZ signals colocalized on SLBs (Fig. S4C), suggesting that these condensates could interact *in vitro* in their physiological topology. Full-length SpmX-eYFP fusions expressed in *E. coli* exhibited membrane-associated fluorescence signal that became punctate followed by coalescence of these puncta as time progressed (Fig. S5A, SI video 6). One interpretation of experiments showing spherical droplets in solution, reversible puncta on SLBs and puncta fusion in *E. coli*, (with the latter two experiments preserving SpmX's physiological orientation) is that SpmX condensates form via phase separation in their physiological topology. Finally, we compared SpmX concentration in *Caulobacter* to those used for *in vitro* experiments. The number of SpmX molecules in the polar region was measured by dividing the total polar fluorescence intensity of SpmX-eYFP in *Caulobacter* cells by the mean fluorescence intensity of single SpmX-eYFP molecules (Supplementary text) *(23, 24)*. The number of SpmX molecules (average 58 molecules/pole) (Fig. S6A, left, detailed analysis in supplementary text) roughly corresponds to ~100-fold higher concentrations than the maximum concentrations at which SpmX phase separated *in vitro* (Fig. S2C). Given the requirement of a lower critical concentration for phase separation, and that crowding promotes phase separation (Fig.

S2A), these data support the notion that SpmX exists as a phase-separated condensate interacting with the PopZ condensate at the *Caulobacter* stalk-bearing pole.

The trans-membrane DivJ histidine kinase (Fig. 2A) has been shown to localize to the stalk-bearing pole by virtue of its binding to SpmX *(15, 16)*. To investigate if the SpmX-IDR, and consequently SpmX phase separation, influence DivJ polar localization, we used DivJ diffusion as a proxy for DivJ-SpmX interaction. Accordingly, we performed three-dimensional (3D) single-molecule tracking of DivJ, endogenously tagged with Halo enzyme and labeled using Janelia Fluor 549 (JF549-HaloTag) in the presence of either wild type (WT) SpmX, SpmXΔIDR, or a *spmX* deletion (ΔSpmX) (Fig. 2B,C) *(25)*. The DivJ-Halo enzyme construct was under the control of the native *divJ* promoter and fully complemented a Δ*divJ* strain. 3D imaging in WT cells revealed polar trajectories as well as membrane associated non-polar trajectories, assessed from their curvature (Fig. 2B, right panel, black dashed lines show curvature). While 60% of all the DivJ trajectories were observed at the pole in WT cells, this number dropped to 10% in ΔSpmX cells, owing to the loss of interaction between DivJ and SpmX (Fig. S6B). In cells containing only SpmXΔIDR, we observed a three-fold decrease in the frequency of polar DivJ trajectories (20% of all trajectories observed at the pole) when compared to WT cells. These results suggest that the SpmX-IDR mediates an interaction with DivJ *in vivo*, in agreement with reported *in vitro* biochemical data *(16)*. Owing to the small polar diffusivities and limited trajectory lengths, we analyzed DivJ tracks using the cumulative distribution function (CDF) of displacements in 20 ms time intervals *(26, 27)*. CDF analyses showed that DivJ displacements in the polar microdomain were greater in both ΔSpmX and SpmXΔIDR cells and smaller in WT cells (Fig. 2D), consistent with the observation that SpmX, and specifically the SpmX-IDR, increase DivJ's residence time at the pole.

These results were also supported by mean-squared-displacement (MSD) analyses showing that DivJ diffusion is ten-times faster in the polar microdomain in the absence of SpmX-IDR. However, the difference between diffusion constants was not statistically significant owing to the limitations posed by short trajectories in space and time (Fig. S7A). As a control, we engineered a Halo enzyme fused to the trans-membrane helical region from an *E. coli* sensor protein ArcB, such that the resulting fusion does not interact with SpmX or any other proteins in *Caulobacter*. The membrane localized Halo

enzyme displayed the same diffusivity in the pole in the presence or absence of SpmX (Fig. S7B) indicating that the differences in diffusion observed for DivJ are specific to its interaction with SpmX. Cumulatively, single molecule diffusion analyses indicate that DivJ is localized to the *Caulobacter* stalk-bearing pole through an interaction that is facilitated by the SpmX-IDR, resulting in a higher dwell time and concentration of DivJ in the polar membraneless organelle. Together with previous data, these results establish a modular role of SpmX, where SpmX polar localization is mediated by an interaction between SpmX Lysozyme homology domain (aa 1-155, Fig. 1D) and PopZ *(16)*. Next, the SpmX-IDR facilitates an interaction with DivJ *(16)* leading to DivJ's polar sequestration that is further enhanced via SpmX phase separation.

Strains in which *spmX* has been deleted exhibit a dramatic decrease in DivJ phosphorylation and compromised viability *(15)*. We hypothesized that DivJ sequestration to the SpmX condensate regulates DivJ kinase activity. Accordingly, we measured DivJ phosphorylation levels *in vivo* in WT, *ΔspmX,* or *spmXΔIDR* strains using radiolabeled ATP and immunoprecipitation (Fig. 2E). Compared to WT cells, SpmXΔIDR strains exhibited about 80% decrease in the levels of phosphorylated DivJ, similar to decrease observed in the *spmX* deletion strain (Fig. 2E). The dependence of DivJ kinase activity on SpmX-IDR could either be a result of DivJ sequestration within the SpmX condensate, or a direct conformational regulation of its catalytic domains by the SpmX-IDR. To address this, we tested if DivJ exhibits concentration dependent activity in its physiological topology by tethering the cytoplasmic domains of DivJ (189-597, DivJ(ΔTM), Fig. 2A) to liposomes *in vitro* via an N-terminal His_6-Tag. Liposomes contained 90% di-oleoyl-phosphatidyl glycerol (DOPG) by mass to mimic the lipid composition of *Caulobacter's* negatively charged membrane. The remaining 10% was composed of nickel-chelated lipids (DGS-NTA) to bind His_6-DivJ(ΔTM). DivJ concentration was kept constant in these assays while decreasing the liposome concentration by weight. The decrease in liposome concentration led to an increase in DivJ density per liposome. Upon varying the density of DivJ from ~3 molecules to ~300 molecules (Supplementary text) we noticed a sharp, density dependent increase in DivJ activity that saturated at ~20-50 molecules per liposome (Fig. 2F). To compare DivJ density on liposomes to that in the polar microdomain in *Caulobacter*, we measured polar fluorescence from cells expressing

DivJ-eYFP (under the native *divJ* promoter and fully complementing Δ*divJ* strain) and divided the resulting intensity distribution by the intensity of single DivJ-eYFP molecules. On an average, we counted 11 molecules of DivJ per pole (Fig. S6A, right) suggesting that DivJ's optimal kinase activity is achieved at a similar density at the cell pole as measured *in vitro* on liposomes (blue dashed line in Fig. 2F).

Finally, we investigated the effect of SpmX phase separation on DivJ density in an *E. coli* heterologous expression system. *E. coli* (BL21(DE3)) cells expressing SpmX-eYFP and DivJ-eCFP under the control of a T7 promoter were induced using 100 µM Isopropyl β-D-thiogalactoside (IPTG) followed by confocal microscopy. DivJ-eCFP colocalized with the SpmX-eYFP puncta, implying that SpmX phase separation may increase DivJ's local density (Fig. 2G, left panel). DivJ fluorescence in cells exhibiting punctate SpmX signal was compared against cells that exhibited a diffuse SpmX signal (Fig 2G, right panel). The analysis shows that the difference between localized and diffuse DivJ fluorescence signal in cells exhibiting SpmX puncta can range between two to ten-fold higher compared to cells were SpmX and DivJ are diffuse (Fig. 2G, top panel). Considering punctate signal as a proxy for SpmX phase separation, the analyses support the idea that SpmX phase separation acts to concentrate DivJ within SpmX condensates. While an additional, direct regulatory role of the SpmX-IDR cannot be ruled out, our data suggest that SpmX-IDR contributes to SpmX phase separation, which in turn functions to concentrate the low number of DivJ molecules to the SpmX condensate, thereby enhancing DivJ kinase activity. It has been recently suggested that phase separation may act to buffer cellular noise *(28)*. Given the low copy numbers of DivJ at the pole, SpmX phase separation may serve a similar function, buffering large fluctuations in DivJ concentration that may otherwise disrupt signaling and cell cycle progression.

Given that phase transitions are sensitive to their surroundings, we asked if the critical DivJ kinase signal modulation in *Caulobacter* is responsive to metabolic fluctuations in the environment. Intracellular ATP is not only a key metabolite but is also a regulator of cytoplasmic viscosity *(29)*, macromolecular diffusion *(30)* and a biological hydrotrope that has been shown to solubilize protein condensates *(31)*. While ATP is a substrate for DivJ phosphorylation, which is promoted by sequestration within the SpmX condensate, the hydrotrope effect of ATP may also regulate DivJ kinase activity indirectly

by modifying SpmX condensate properties. To explore this possibility, we first determined if ATP at physiological concentrations affects the physical properties of PopZ and SpmX condensates. Titration of PopZ and SpmX condensates against a physiologically relevant ATP concentration range *(32) in vitro*, showed that PopZ condensates dissolved in 0.5-2mM ATP, whereas SpmX condensates were soluble above 1mM ATP concentrations (Fig. 3A and Fig. S8A). Given that crowding promotes phase separation (Fig. S2A), we observed that the presence of crowding agents such as Poly-ethylene glycol (PEG-6k) opposed the hydrotrope effect of ATP on PopZ and SpmX condensates (Fig. S8B). Protein titrations against ATP and experiments performed with PEG-6k revealed short-lived intermediate states reminiscent of detergent bubbles or micelles (Fig. 3A, PopZ, 0.1mM; SpmX (ΔTM), 1mM and Fig. S8B, PEG conditions). Fluorescence microscopy data showed that these protein bubbles were dynamic (SI video 7), could be captured at different sizes based on ATP concentration (Fig. S8D), and could form in the presence of other hydrotropes such as ADP and APPNP (Fig. S8E). Two-color confocal microscopy of condensates with SpmX and DivJ, incubated with 1mM ATP, showed that at equilibrium, DivJ preferentially sequestered in the condensate phase with SpmX, supporting the observation that SpmX phase separation acts to concentrate DivJ (Fig. S8F). Diffusion of SpmX and importantly, DivJ, depended on the phase in which it partitioned with SpmX implying that ATP can change DivJ diffusion in SpmX condensates (Fig. S8G). Cumulatively, these results argue that SpmX phase separation concentrates and stimulates DivJ kinase activity while the hydrotrope effect of ATP modulates SpmX phase separation and sequestration of DivJ within the condensate.

Based on these observations *in vitro*, we asked if the hydrotrope effect of ATP regulates PopZ and SpmX concentrations in their respective condensates at the *Caulobacter* pole. To test this hypothesis, we measured the mean polar fluorescence signal from *Caulobacter* cells expressing mCherry-PopZ and SpmX-eYFP upon treatment with the ionophore Carbonyl cyanide m-chlorophenyl hydrazone (CCCP), which rapidly depletes the cells of ATP as measured by a Luciferase based assay *(33)* (Fig. S9A). The mean polar fluorescence serves as a proxy for the concentration of the proteins at the pole. We observed an increase in the mean PopZ polar signal in the presence of CCCP, which implies that the concentration of PopZ in the condensate phase is higher under low

ATP conditions (Fig. 3B), in agreement with the observations *in vitro* (Fig. 3A). We did not detect a significant difference in SpmX signal under the same conditions (Fig. S8C), likely due to the low copy number of SpmX at the pole (Fig. S6A, left).

To overcome this limitation and observe the effect of ATP on SpmX independent of PopZ in a living cell, we over-expressed SpmX in the *E. coli* heterologous expression system. SpmX-eYFP or DivJ-eCFP were expressed on a low-copy plasmid under the control of a T7 promoter in *E. coli* (BL21(DE3)) and intracellular ATP was varied by changing the glucose concentration in minimal growth medium (Fig. S9B). *E. coli* cells expressing SpmX-eYFP or DivJ-eCFP were grown in M9 medium supplemented with glucose (M9G) and protein expression was induced by the addition of IPTG. Following induction, the cells were washed and shifted to three different media. Intracellular ATP levels (measured using a Luciferase based assay) *(33)* in *E. coli* shifted to M9 media (lacking a carbon source) dropped to 53% of the ATP levels measured in *E. coli* shifted to M9G (Fig. S9C). To obtain high crowding conditions that promote phase separation, cells were shifted to M9 medium supplemented with glucose and a non-polar osmolyte, Sorbitol (M9GS) *(34)*. In *E. coli*, phase separating membrane proteins appear as a non-uniform or punctate signal while an absence of phase separation is marked by a uniform membrane associated fluorescence signal (Fig. S5A and SI video 6). SpmX-eYFP when expressed alone and shifted to M9G (high ATP) showed a relatively uniform membrane associated signal (Fig. 3C, middle panel, blue line) as would be expected for a decrease in phase separation. Upon exposure to decreased levels of intracellular ATP in cells shifted to M9 media, *E. coli* displayed a non-uniform membrane fluorescence of SpmX-eYFP, evident from line profile across the cell length (Fig. 3C, left panel, blue line), indicative of an increase in phase separation. SpmX-eYFP expressing cells shifted to M9GS exhibited a more dramatic punctate signal (Fig. 3C, right panel, blue line), consistent with the role of crowding in promoting phase separation. In stark contrast, DivJ-eCFP expressed alone remained diffuse under all three media conditions irrespective of ATP or crowding levels, consistent with its lack of phase separation *in vitro* (Fig. 3C, red lines).

To observe the colocalization pattern of SpmX and DivJ, we co-expressed SpmX-eYFP and DivJ-eCFP on a low copy plasmid under the control of a T7 promoter in the

same *E. coli* cells. Protein expressions and media challenge were carried out as in the previous experiment (Fig. 3C). Cells shifted to M9G (high ATP) exhibited a largely diffuse but correlated signal for SpmX-eYFP and DivJ-eCFP (Fig. 3D, middle panel). Cells with reduced intracellular ATP concentrations in M9 media or high crowding in M9GS media, displayed a punctate and correlated fluorescence signal in both channels, albeit at a higher puncta intensity compared to the M9G case (Fig. 3D, left and right panels, respectively). We also observed polar accumulation of proteins under conditions that induce phase separation (Fig. 3D, left and right panels). Polar accumulation can most likely be explained by the propensity of self-associating proteins to accumulate at regions with negative curvature, such as the pole, as has been demonstrated for DivIVA in *B. subtilis (35)*. Together, these results imply that the hydrotrope effect of ATP and molecular crowding act antagonistically to control phase separation of proteins either by solubilization of IDR containing proteins (hydrotrope effect of ATP) or phase separation into condensates (molecular crowding) in living bacteria. The DivJ kinase colocalizes with SpmX under all three growth conditions, with a higher DivJ signal observed within SpmX condensates under low ATP or high crowding conditions. Such an increase in localization may enhance DivJ's local concentration and density dependent kinase activity (Fig. 2F).

DivJ is a key component of a phospho-signaling pathway that modulates the phosphorylation, and thus activity of CtrA, a central transcription factor controlling *Caulobacter* cell cycle progression *(20)*. Thus, a decrease in phosphorylated DivJ concentration in pre-divisional cells leads to an aberrant accumulation of CtrA~P, resulting in multiple cell cycle defects *(19)*. A DivJ mutant unable to catalyze its own phosphorylation (H338A) exhibits slow growth and aberrant cell division, resulting in long cells (Fig. 4A) *(19, 36)*. To determine the contribution of the SpmX-IDR motif to cell growth, we grew WT and SpmXΔIDR strains in minimal media with decreasing glucose concentrations as a proxy for decreasing intracellular ATP levels (Fig. 4B). We observed a difference in doubling times (1 hour increase) between WT and SpmXΔIDR strains in minimal media with 1mM glucose ($M2G_{1mM}$). However, upon growing cells in M2 with 0.5mM glucose, we observed a 3 hour difference in doubling times in SpmXΔIDR cells compared to WT cells. This phenotype was significantly enhanced in M2 with 0.2mM glucose resulting in SpmXΔIDR cells doubling ~10 hours slower than WT cells under the

same conditions (Fig. 4B). Thus, the SpmXΔIDR cells grown under low glucose conditions phenocopy a DivJ mutant lacking its kinase activity with respect to growth rate. To assess the effect of intracellular ATP on cell division in WT and SpmXΔIDR cells, we grew cells in minimal media with varying glucose concentrations, measured intracellular ATP levels using a Luciferase based assay *(33)*, and imaged the same cells by phase contrast microscopy (Fig. 4C, D). We observed an increase in the percentage of long cells (aberrant cell division) in the SpmXΔIDR strain (phenocopying DivJ kinase mutant) compared to the WT strain (Fig. 4C, D), concomitant with a decrease in intracellular ATP concentrations (red bars, Fig. 4D), as glucose concentration in the media was lowered. This result suggests that the hydrotrope effect of ATP modulates SpmX phase separation and hence DivJ activity within the condensate in response to glucose availability to *Caulobacter* cells.

Cells that lack the SpmX-IDR motif can localize only a third of DivJ to the pole compared to wild type cells (Fig. S6B). In these cells, DivJ phosphorylation is controlled only by ATP concentrations and not by SpmX phase separation (Fig. 4E). Therefore, when the substrate (ATP) concentrations are high, even with a depleted DivJ polar concentration, DivJ phosphorylation may be sufficient for CtrA dephosphorylation. However, If the substrate (ATP) is depleted in SpmXΔIDR cells, the lower DivJ polar concentration may not suffice for optimal kinase activity, due to a lack of SpmX-IDR driven sequestration under low ATP conditions (Fig. 4E). As a result, cells lacking DivJ sequestration by SpmX phase separation (SpmXΔIDR) phenocopy WT cells under high ATP conditions but deviate towards a DivJ kinase mutant, as ATP is reduced. These results indicate that SpmX phase separation enhances DivJ concentration to maintain robust kinase activity in low intracellular concentrations of ATP (Fig. 4E), and that this regulation is lost in the absence of the SpmX-IDR motif. However, under nutrient rich conditions, the abundance of ATP ensures optimal kinase activity irrespective of the regulation via SpmX-IDR (Fig. 4E).

Taken together, our work establishes distinct roles of disordered polar proteins in kinase regulation in an oligotrophic bacterium that is devoid of membrane-bound organelles. First, SpmX localizes to the stalk-bearing pole through an interaction between its structured domain and PopZ *(16)*, establishing two interacting biomolecular

condensates that form via phase separation. SpmX, in turn, interacts with the DivJ kinase *(16)* and concentrates it within the SpmX condensate at the cell pole, thereby enhancing DivJ's density dependent kinase activity. Finally, the physical properties of the SpmX condensate, and diffusion of its client DivJ within the condensate, are modulated by intracellular levels of ATP. This ATP dependent tunability of the SpmX condensate serves as a mechanism for robust regulation of DivJ phosphorylation under glucose-limited conditions. While certain eukaryotic cells and symbiotic bacteria often thrive in tissues and cells in relatively stable environments, free-living bacteria are constantly exposed to chaotic famine and feast cycles *(37)*. Therefore, co-option of an interaction between an IDR and a low copy number kinase ensures that under dilute nutrient conditions that are typical in the wild, SpmX phase separation enables optimal sequestration and activity of the kinase. This idea supports a framework where the degree of cooperativity of an enzyme regulated by phase separation is a variable function of substrate (ATP) concentration as opposed to a constant (such as the Hill coefficient), due to the hydrotrope effect of ATP. Such a mechanism ensures optimal cooperativity between low copy number enzymes over a broad range of substrate concentrations in the cell. Our work raises the possibility that IDRs and the hydrotrope effect render a robustness to ATP dependent kinase signaling. Given that ATP can diffuse much faster in a cell compared to gene expression time scales, condensates regulated by the hydrotrope effect may adapt swiftly and robustly to changing metabolic conditions. Thus, it remains to be seen whether the diverse repertoire of hydrotropes and IDRs in bacteria *(38)* may serve as a universal control knob to tune reactivity in response to the environment and metabolic state of a cell.

Figures – Main text

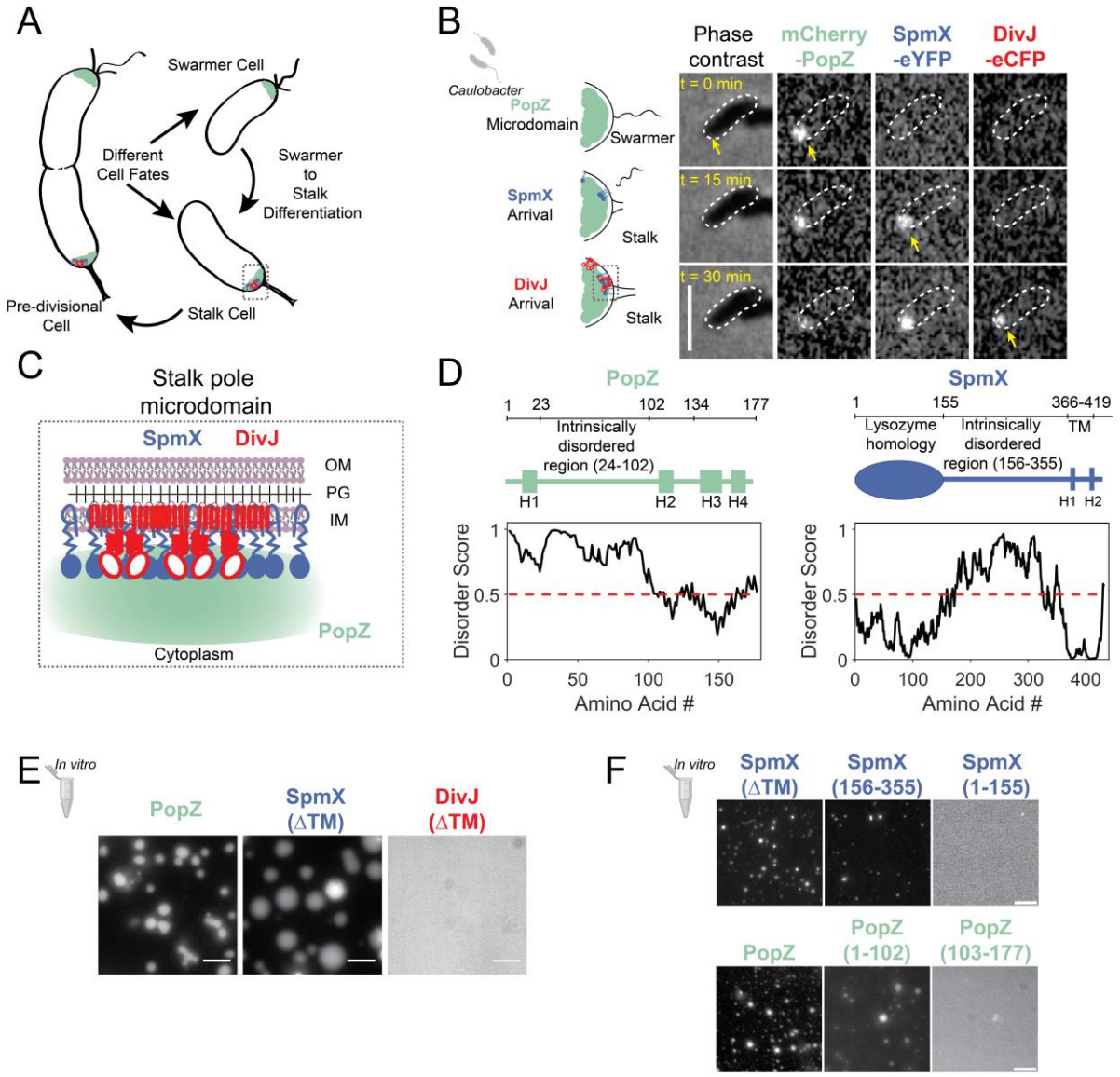

Figure 1. *A membraneless organelle in Caulobacter forms via phase separation and recruits a kinase to the pole*. A. Summarized *Caulobacter* cell cycle showing the key steps of cell division and subsequently, differentiation from swarmer to stalked cell. Shown here is the polar location of the PopZ (green), SpmX (blue), and the DivJ kinase (red) as a function of the *Caulobacter* cell cycle. SpmX and DivJ localize to the PopZ microdomain only at the stalk-bearing pole. B. Fluorescence images showing the sequential arrivals of SpmX-eYFP and DivJ-eCFP to the polar microdomain containing mCherry-PopZ. Arrows indicate the differentiating pole during the swarmer to stalked cell transition and the sequential appearance of mCherry-PopZ, SpmX-eYFP, and DivJ-eCFP foci in the

fluorescence images. Cell bodies are outlined by a dashed white line (scale bar 2µm). C. Organization of membrane bound DivJ and SpmX proteins with respect to the polar PopZ microdomain. OM: Outer membrane, PG: Peptidoglycan, IM: Inner membrane. D. Domain organization and disorder prediction scores for the PopZ and SpmX amino acid sequences from IUPred *(39)*. E. Fluorescence images of labelled recombinant PopZ (full length, Atto488), SpmX (ΔTM, Cy3) and DivJ (ΔTM, Atto488) (protein concentration 5µM) showing that PopZ and SpmX, but not DivJ, phase separate *in vitro* (scale bar 5µm). F. Fluorescence images of purified variants of SpmX and PopZ. Top. SpmXΔTM (aa 1-355) and SpmX-IDR (aa 156-355) alone phase separate *in vitro,* but not SpmXΔIDR (aa 1-155). SpmX ΔTM and SpmXΔIDR were tagged using Cy3 while SpmX-IDR alone contains an N-terminal eYFP fusion. Bottom. PopZ (Atto488) and PopZ-IDR (aa 1 – 102) (Atto488) phase separate *in vitro* but not PopZ ΔIDR (aa 103-177). For both SpmX and PopZ, the IDR is necessary and sufficient for phase separation *in vitro*. All proteins in panel F are at a concentration of 1µM (scale bar 2µm).

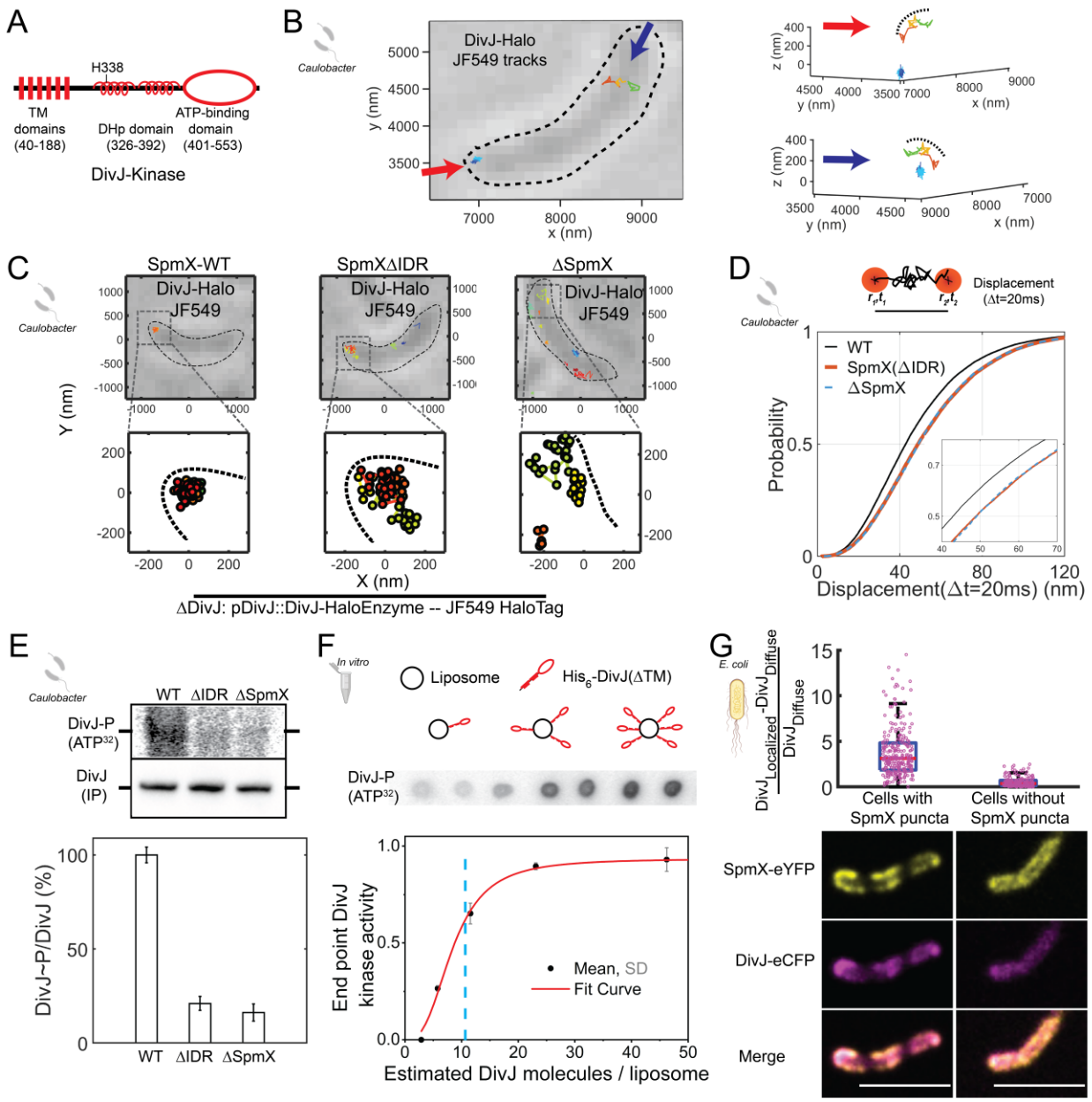

Figure 2. *DivJ exhibits a density dependent kinase activity that is stimulated by binding to SpmX, and sequestration in the polar microdomain.* A. Diagram of the DivJ kinase domains indicating the six trans membrane domains (TM), the catalytic DHp domain, and the ATP-binding domain. B. 3D single-molecule trajectories in *Caulobacter* cells expressing an endogenous DivJ-Halo enzyme fusion, labeled with JF549-HaloTag ligand. Left. A bright-field image of a live *Caulobacter* cell, overlaid with 2D projections of 3D DivJ trajectories measured using single-particle tracking. Each trajectory is plotted using a different color. Arrows denote perspectives for the 3D representation shown on the right.

Right. Representation of the trajectories from the left panel in 3D space with appropriate perspective and all three Cartesian axes. Green and red trajectories in the body are membrane-associated as can be seen from their curvature, highlighted using a black dashed line. C. Representative single-molecule trajectories of endogenous DivJ-Halo enzyme fusion labeled using JF549-HaloTag dye in strains bearing different SpmX perturbations. Top: individual DivJ trajectories overlaid on a bright-field image of a *Caulobacter* cell. Bottom: a zoomed in view of the polar trajectories (for WT-SpmX and SpmXΔIDR) and non-polar trajectories (for ΔSpmX). Each trajectory is shown as a 2D projection and in a different color. D. Cumulative distribution function of displacements obtained from DivJ trajectories in 20ms in respective SpmX background strains. Inset shows a zoomed in view of the graph highlighting the overlapping CDFs for SpmXΔIDR and ΔSpmX. Number of polar DivJ trajectories analyzed is 974, 443 and 291, for WT, SpmXΔIDR and ΔSpmX cells, respectively. E. *In vivo* phosphorylation measurement of DivJ in different SpmX perturbations. DivJ phosphorylation levels in the bar plot are expressed as a ratio of DivJ~P (intensity in the top gel (ATP(γ–^{32}P)) to DivJ concentration (immunoprecipitation using an antibody against DivJ)) and are normalized to the ratio observed in WT cells. Error bars denote standard error of the mean from three biological replicates. F. DivJ auto-kinase activity assayed on liposomes. A fixed concentration of 5 μM His_6-DivJ(ΔTM) was pre-incubated with increasing amounts of liposomes to obtain surface densities ranging from ~3 to 50 His_6-DivJ(ΔTM) molecules per liposome. Kinase reaction was performed using ATP(γ–^{32}P) and samples were assayed by blotting on a nitrocellulose membrane followed by phosphor imaging. The activity of each His_6-DivJ(ΔTM) surface density state is normalized to the highest density condition. Representative phosphor imaging data from spot assays is shown above the graph. Intensity from spots was quantified and the data were fit to a Hill-Langmuir curve as described in the methods section. Dashed blue line represents the physiological polar DivJ concentration of 11 molecules measured from the assay in Fig. S6A. G. Confocal micrographs of a single BL21(*DE3*) cell co-expressing SpmX-eYFP and DivJ-eCFP fusions under the control of a T7 promoter. After washing the inducer cells are placed on an agarose pad made with M9. The cell in the left panel is imaged 2 hours after placing on the agarose pad while the cell in the right panel is imaged within 5 minutes of placing

on the agarose pad. Both cells are from the same culture and induced using 100µM IPTG for 1h. Punctate membrane-associated signal is interpreted as a proxy for phase separation. Quantification of DivJ signal within cells that exhibit SpmX puncta (left) or that do not have puncta (right) is shown in the box plot on top. The DivJ signal is expressed as a difference between localized and diffuse signal in a cell, normalized by the mean diffuse signal in the cell. For cells without any puncta, the difference in the numerator is from two different points in a single cell. Each point on the plot denotes an average from 10 cells. A total of 2750 cells containing SpmX puncta, and 1870 cells with diffuse SpmX signal were analyzed (scale bar 5µm).

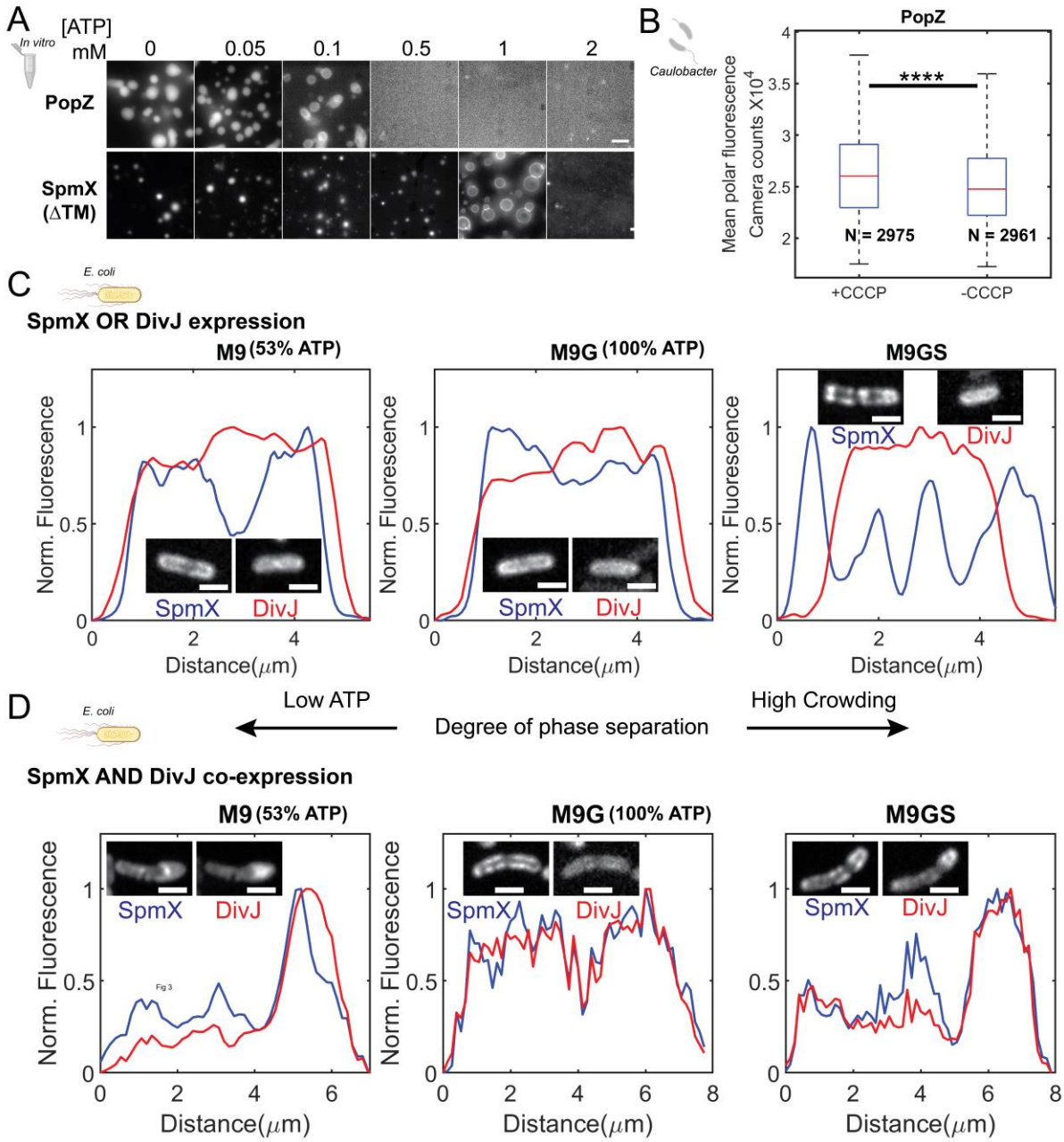

Figure 3. *ATP acts as a hydrotrope for PopZ and SpmX condensates.* A. Fluorescence micrographs showing *in vitro* titration of fluorescently-labeled PopZ (Atto488) and SpmXΔTM (Cy3) against ATP concentrations ranging from 0 to 2mM. The formation of phase separated droplets was inhibited at 0.5 mM ATP for PopZ and 2 mM for SpmX(ΔTM). Protein samples at 5μM were incubated with ATP at indicated concentrations at room temperature for 2 hours followed by fluorescence microscopy. Brightness and contrast for each image was adjusted to better highlight the cases where

no condensates are observed (scale bar 5µm). B. Box plot showing average polar fluorescence signal from *Caulobacter* cells expressing mCherry-PopZ as the sole protein copy. Cells were grown in M2G and split into two tubes, one treated with 100 µM CCCP in DMSO and the other treated with an equivalent volume of DMSO for 10 mins. Red lines denote the median values and N is the number of cells analyzed to obtain the data. Asterisk denote $p<0.0001$ based on a two sample t-test. C. Confocal fluorescence micrographs of *E. coli* (BL21(DE3)) expressing either SpmX-eYFP or DivJ-eCFP under the control of a T7 promoter in different media conditions. Protein expression was induced using 100µM IPTG for 1 hour, cells were washed and incubated in different media: M9, M9-Glucose (M9G) or M9-Glucose supplemented with 0.5M Sorbitol (M9GS) for 2 hours. The relative ATP concentrations measured for M9 and M9G using a commercial Luciferase based assay (BacTiter Glo) are reported in parentheses (See Fig. S9C). Phase separation of proteins appears as a non-uniform or punctate fluorescent signal as shown by the line profiles for SpmX (blue lines) in the M9 (low ATP) or the M9GS (high crowding) conditions. Under M9G incubation (high ATP), SpmX signal is relatively uniform on the membrane. DivJ-eCFP, when expressed alone, shows uniform membrane signal irrespective of the media conditions (red lines). Line profiles are measured using the entire length of the cell shown as distance between the two cell poles (scale bars 2µm). D. Confocal fluorescence micrographs of *E. coli* (BL21(DE3)) co-expressing SpmX-eYFP and DivJ-eCFP under the control of a T7 promoter in the indicated media conditions. Protein expression, media incubation and ATP measurements were performed as in (C). In this case DivJ-eCFP signal (red line) colocalizes with SpmX-eYFP (blue line) signal under all conditions. However, the signal is more punctate for low ATP(M9) or high crowding conditions (M9GS) as shown by the line profiles from single cells in each case (scale bars 2µm).

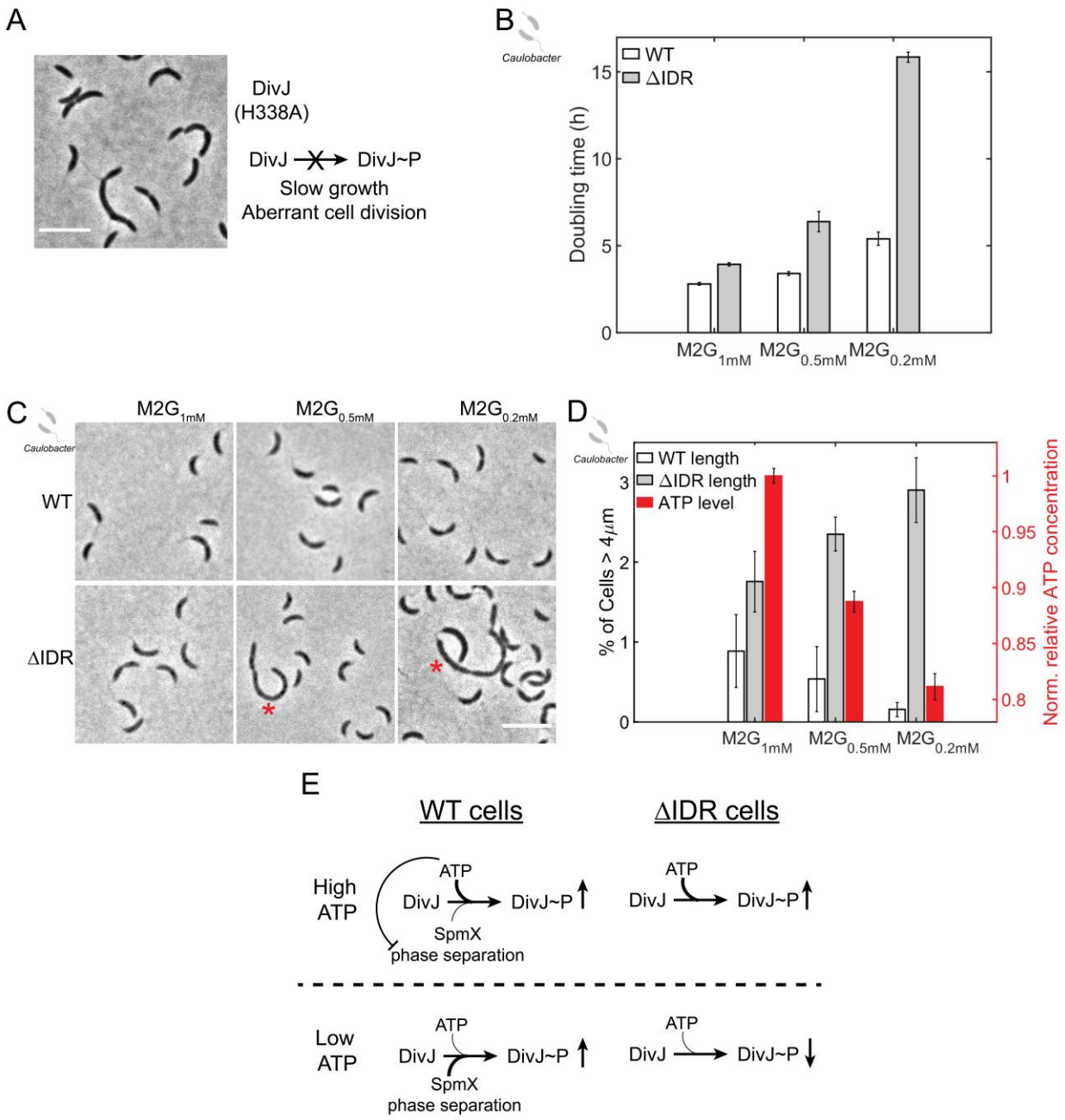

Figure 4. *Hydrotrope effect regulates DivJ signaling via SpmX phase separation in response to intracellular ATP concentrations.* A. Phase contrast image of DivJ (H338A) cells in which DivJ phosphorylation cannot occur, leading to the long cell phenotype (scale bar 5µm). B. Doubling time as a function of the growth medium for WT and SpmXΔIDR cells. Subscripts for minimal media denote the glucose concentration in the media. Doubling times were calculated by averaging at least three time lags during which the OD doubled in the exponential growth phase. Each measurement was performed in triplicate.

Error bars represent standard error of the mean. C. Phase contrast images of WT (top panel) and SpmXΔIDR (bottom panel) cells grown in defined minimal medium (M2) with varying amounts of glucose (denoted by subscript). Asterisk denote the long cell phenotype observed in these cells (Scale bar 5µm). D. (Left axis) Bar plot showing percentage of cells longer than 4µm observed in the WT or SpmXΔIDR strains under decreasing glucose conditions in minimal media. These data are from 3 biological replicates with total of 1800-2000 cells analyzed for each glucose condition. Error bars represent standard error of the mean. (Right axis) Bar plot showing the relative intracellular ATP concentrations in minimal media with decreasing amounts of glucose (indicated by the subscript) from 1mM to 0.2mM. ATP concentrations were measured for the same cells that were imaged using a commercial Luciferase based luminescence assay. Error bars represent standard error of the mean from 3 biological replicates each assayed in triplicate. E. A potential model for SpmX regulation of DivJ. DivJ phosphorylation is regulated by ATP concentrations and SpmX phase separation in WT cells. Under high ATP conditions the role of SpmX phase separation is abrogated due to the hydrotrope effect of ATP (top, left). Under low ATP conditions, SpmX phase separation is promoted, and modulates DivJ activity (bottom, left). In the absence of SpmX-IDR, DivJ regulation is controlled solely by ATP concentrations. Under high ATP concentrations, DivJ activity may be sufficient (right, top, upward facing arrow) but under low ATP concentration, DivJ activity may be diminished (shown by downward facing arrow).

Acknowledgements

The authors thank Drs. Harley McAdams, Kotaro Fujii, Dante Ricci, Edward de Koning and Bo Gu for a careful reading of the manuscript. The authors also thank Dr. Sean Crosson and Dr. Sunish Radhakrishnan for helpful discussions. The authors thank all members of the Shapiro and Moerner labs for their help with useful discussions throughout this work. This work was supported by the National Institute of General Medical Sciences, the National Institutes of Health (R35-GM118071 to L.S.), and (R35-GM118067 to W.E.M.). L.S. is a Chan Zuckerberg Biohub Investigator.

Note: The *E. coli*, *Caulobacter* and centrifuge tube icons in each figure are created using Biorender.com.

Supplementary Information

1. Characterization of protein phase separation

PopZ and SpmX both contain Proline rich IDRs (~80 and 200 amino acids, respectively, predicted by IUPred *(34)*) that are necessary and sufficient for phase separation. PopZ has previously been observed to form fibrils *in vitro (14)*. Reconstitution of PopZ and SpmX in solution showed that they assembled into spherical condensates, reminiscent of those formed by liquid-liquid phase separation (Fig. 1E). To test whether we could observe any structure for these phase-separated condensates we performed transmission electron microscopy on these samples. While we observed near-spherical proteinaceous condensates for SpmX in the presence or absence of the crowding agent PEG-6k, PopZ condensates could only be observed in the presence of crowding in negative stain electron microscopy (Fig. S1). Additionally, PopZ condensates were more fibrillar compared to SpmX, reminiscent partly of the structures observed previously under higher concentrations *(14)*.

We tested the effect of molecular crowding on phase separation of PopZ and SpmX since molecular crowding enhances self-association rates of proteins. In line with this idea and previous results for other IDRs, we observed that addition of a crowding agent such as PEG-6k led to an enrichment of the proteins in the condensates (Fig. S2A). Phase-separated condensates are in a state of chemical equilibrium and their formation is reversible. To test for reversibility *in vitro*, we formed PopZ or SpmXΔTM condensates at 5µM in buffer (50mM HEPES-KOH, pH7.2) without salt and then added 0.5M KCl. Upon addition of KCl, PopZ condensates dissolved more rapidly compared to SpmX condensates (Fig. S2B, SI video 1, 2). Additionally, SpmX condensates did not dissolve completely under these conditions and reached a new equilibrium in 20 minutes (SI video 2). Since PopZ and SpmX-IDRs have an abundance of charged amino acids, we tested if they exhibit a response to changes in tonicity. For this, we dialyzed the proteins against buffers (50mM HEPES-KOH, pH7.2) containing different salt (KCl) concentrations and imaged the resulting solution by fluorescence microscopy (Fig. S2C). We found that PopZ (full length) did not phase separate under 100nM concentration for all salt conditions. However, SpmXΔTM phase separated under all protein and salt conditions tested.

Protein diffusion in condensates is a measure of self-interaction between the condensate-forming proteins. We used FRAP to observe the diffusion of labeled PopZ and SpmX in their condensates. Full length PopZ incubated in reaction buffer (50mM HEPES-KOH, 0.1M KCl) displayed negligible recovery while the IDR containing domain of PopZ (AA1-102) displayed 40% recovery under the same conditions (Fig. S3A). This is in line with previous results showing that a part of this region (23-102) fails to oligomerize *in vivo* owing to weak interactions *(11)*. Similarly, SpmX (SpmXΔTM) exhibited stronger inter-molecular interactions (negligible recovery) compared to SpmX-IDR alone (AA156-355) in the condensates (Fig. S3B). These results indicate that intermolecular interactions in SpmX and PopZ condensates are driven both by the IDR and the structured domains. Strong intermolecular interactions between PopZ or SpmX within their respective condensates are also revealed by observing their growth in time (SI video 3, 4). Fluorescently-tagged condensates of these proteins grew radially with time, reminiscent of phase separated condensates exhibiting Ostwald ripening *(40)*.

Observation of SpmX or PopZ condensates in *Caulobacter crescentus* poses a major challenge. In the native cellular environment, PopZ forms a space-filling assembly in the cytoplasm, *(17)* while SpmX is a trans-membrane protein. The polar region of *Caulobacter*, where PopZ and SpmX are localized, is a ribosome excluding region *(14)*. High resolution images of SpmX in live *Caulobacter* cells at room temperature appear to be sub-diffraction limited spots localized to the pole *(41)*. Recent correlative single-molecule and cryo-ET data *(18)* show the PopZ microdomain as a dome, resting below, and abutting the membrane at the cell pole. The cytoplasmic interface at the base of the dome is a membraneless boundary. The trans-membrane SpmX proteins cluster to a defined region on the side of the PopZ microdomain at the base of the stalk. Based on these observations, the topological arrangement of SpmX is a critical consideration in characterizing the properties of the SpmX condensate. While *in vitro* experiments with PopZ in solution reflect the condensate characteristics of this cytoplasmic protein, we sought to further verify phase separation of SpmX, which is a membrane protein with a two-dimensional topology. Accordingly, we observed the formation of fluorescently-labeled SpmX condensates on a supported lipid bilayer (SLB) that closely mimicked the negatively charged lipids found in *Caulobacter (42),* containing 0.1% Ni-NTA headgroup

lipids for tethering His-tagged SpmXΔTM. We anchored Cy3-labeled SpmXΔTM(His_{10}) molecules to the SLB via a polyHistidine-tag and observed diffraction-limited to sub-micron sized fluorescent puncta on the SLBs (Fig. S4A). To validate whether these puncta were indeed condensates, we tested for reversibility by adding salt to the flow cells. Upon addition of 0.25 M KCl, we observed complete dissolution of SpmX condensates within 10 minutes (SI video 5), demonstrating that the observed puncta exhibited properties of SpmX condensates observed in solution (Fig. S4B). To determine if these condensates form on the SLB while preserving protein interactions, we incubated PopZ (Atto488 labeled) in the flow cell containing SLBs with SpmX condensates. Fluorescence microscopy revealed colocalization of the PopZ and SpmX signal, showing that PopZ could form a complex with SpmX condensates in a physiologically relevant topology (Fig. S4C). Condensates larger than 2µm were observed very rarely in this assay, which limited its utility for further *in vitro* characterization. Increasing the Ni-NTA lipids to obtain larger condensates gave unstable bilayers further limiting this approach for *in vitro* characterization of SpmX condensates.

To characterize SpmX condensates in a living cell, we expressed full length SpmX (with trans-membrane (TM) domains) in *E. coli* as a C-terminal eYFP fusion using a pACYC low-copy plasmid under the control of a T7 promoter. SpmX-eYFP was induced for 1 hour by the addition of 100µM IPTG to cells growing in exponential phase. In cells expressing WT SpmX, microscopic observation on agarose pads revealed a membrane bound signal, confirming the physiological topology of SpmX. We also observed punctate fluorescence signal on the membranes (Fig. S5A). We observed that the fluorescent puncta intensified, and fused with other fluorescent puncta, finally accumulating in regions of high membrane curvature (polar regions) or the mid-cell (in dividing cells) over two hours (SI video 6). A C-terminal eYFP fusion to the SpmX-IDR alone (AA156-431) was unstable when expressed in *E. coli*. However, an N-terminal SpmX-IDR fusion was stable, and we could observe this protein on the *E. coli* membrane, albeit at a much lower degree of phase separation (Data not shown). One interpretation of this result is that interactions mediated via the Lysozyme homology domain also contribute to multivalency of SpmX interactions and therefore, its phase separation. This interpretation is in line with results from *in vitro* solution experiments where we observed weak self-interactions in the IDR

alone condensates (Fig. S3B). To test this possibility in *E. coli*, we performed FRAP on cells expressing WT SpmX and SpmX-IDR alone. We observed a higher recovery of the IDR-alone owing to weaker interactions while negligible recovery from SpmX-WT protein (Fig. S5B), supporting the results from FRAP measurements in solution (Fig. S3B).

Next, we compared protein concentrations used in *in vitro* experiments to physiological protein concentrations in *Caulobacter crescentus*. PopZ is present at ~3500 molecules per C*aulobacter* cell *(10)*, which corresponds to an approximate concentration of ~5mM in the microdomain at the cell pole. PopZ phase separates at concentrations above 100nM *in vitro* (Fig. S2C) suggesting that at physiological concentrations in the cell, PopZ exists in a phase-separated state. We counted the number of SpmX molecules at the *Caulobacter* cell pole *(23, 24)*. On average, we observed 58 molecules of SpmX per pole (Fig. S6A). This number corresponds to a uniform density of 3700 molecules/μm^2 and a concentration of ~1mM (assuming a hemispherical shell with 100 nm radius and a shell thickness of 5nm). These density and concentration numbers are a lower-bound estimate, given that SpmX is not uniformly localized within the PopZ microdomain but rather tightly localized at the base of the stalk, as assessed from correlative Cryo-EM images *(18)*. Further, SpmX phase separation is observed *in vitro* at concentrations as low as 10nM (Fig. S2B). Finally, the enrichment of both PopZ and SpmX in the condensate phase in a crowded environment (Fig. S2A) strongly supports the idea that both PopZ and SpmX exist in a phase separated membraneless organelles at the cell pole.

2. <u>Estimation of number of DivJ molecules per liposome</u>

The estimation of number of DivJ molecules per liposome is based on similar experiments with CckA *(43)* . The goal of this estimation is to assess whether the number of DivJ molecules per liposome is limited by geometrical considerations (area) or concentration of protein and Nickel-NTA sites. To estimate the number of available binding sites for DivJ molecules on a liposome, we calculate the total surface area of the liposome. DOPG liposomes extruded through 100 nm pores have vesicle diameters of 97-106 nm *(44)*, that we approximated as 100 nm for simplification of calculation.

Radius of a 100 nm diameter sphere = 500 Å

Surface area (SA) of a sphere = $4\pi r^2$

SA = 3.14×10^6 Å^2

For 18:1 cis-DOPG, comprising 90% of the lipid mass of the liposomes used in this study, each headgroup occupies 69.4 Å^2 at 20° C and 70.8 Å^2 at 30° C *(45)*

To calculate the number of lipids on the outer layer, we will assume a similar area on average per (69.5 Å^2) lipid despite 10% NTA lipid incorporation.

lipids on the outer membrane = SA / (area per lipid headgroup)

lipids = 3.14×10^6 Å2 / (69.5 Å^2 /lipid) = 4.52×10^4 lipids

There are approximately 45,000 lipid molecules on the outer layer. Of these, 10% (4,500) are DGS-NTA sites for possible DivJ binding.

DivJ loading on liposomes could be limited by either the number of NTA sites or by the total surface area of the liposome.

Calctool.org estimates a 410-residue protein (DivJ (188-597), MW = 43620.70) at 5.2 nm diameter. This calculation assumes that the protein is spherical.

Projecting the sphere down onto the surface of the liposome, we can calculate the surface area of one molecule of DivJ ($A_{protein}$) as a circle of radius ~2.6 nm.

Area of circle (A) = πr^2

$A_{protein}$ = 2,122 Å^2

# of proteins that can bind on the liposome based on area = SA liposome / $A_{protein}$

= 3.14×10^6 Å^2 / 2,122 Å^2 = 1479 protein molecules

Given that ~1,500 proteins can fit by the surface area calculation and there are 4,500 NTA sites available, protein loading on the liposome is surface-area limited.

Next, we determine the molar ratio between DivJ molecules and liposomes. The mass of the lipids in the liposome is equal to the sum of the inner and outer layers of the bilayer.

Bilayer thickness = 3.6 nm

Inner diameter of liposome = 96 nm.

Lipids on inner layer: Inner SA / 69.5 Å^2 = 4.2×10^4 lipids on inner layer

Total lipid molecules (TL) = #lipids inner + #lipids outer layer

TL = $(4.2 + 4.5) \times 10^4 = 8.7 \times 10^4$ lipids/liposome

The liposomes contain 10% DGS-NTA lipids and 90% DOPG lipids by mass. Since the molecular weights of the lipids are similar, we use their mass ratios as a proxy for their molar ratios.

Mass of liposome = (mass NTA lipids) X (#NTA) + (mass DOPG lipids) X (#DOPG)

= (8.7×10^{3} NTA lipids X 1057 g/mol X 1.53×10^{-17} g/liposome) +

(7.9×10^{4} DOPG lipids X 797 g/mol X 1.05×10^{-16} g/liposome)

Total mass of one liposome = 1.20×10^{-16} g

For a 5 µM DivJ sample in a 25 µL volume, we use 8.5 µg protein.

#Liposomes = total mass liposomes / mass per liposome

Let us assume that we add an equal mass of liposomes to the reaction

#Liposomes in reaction = 8.5×10^{-6} g liposomes / (1.2×10^{-16}) g/liposome = 7.1×10^{10} liposomes

#DivJ molecules in the reaction = 7.5×10^{13}

#DivJ molecules per liposome = 1056

This implies that if we add an equal mass of lipid to protein, we reach approximately maximum loading capacity (maximum DivJ molecules per liposome by area = 1100).

Figures – Supplementary text

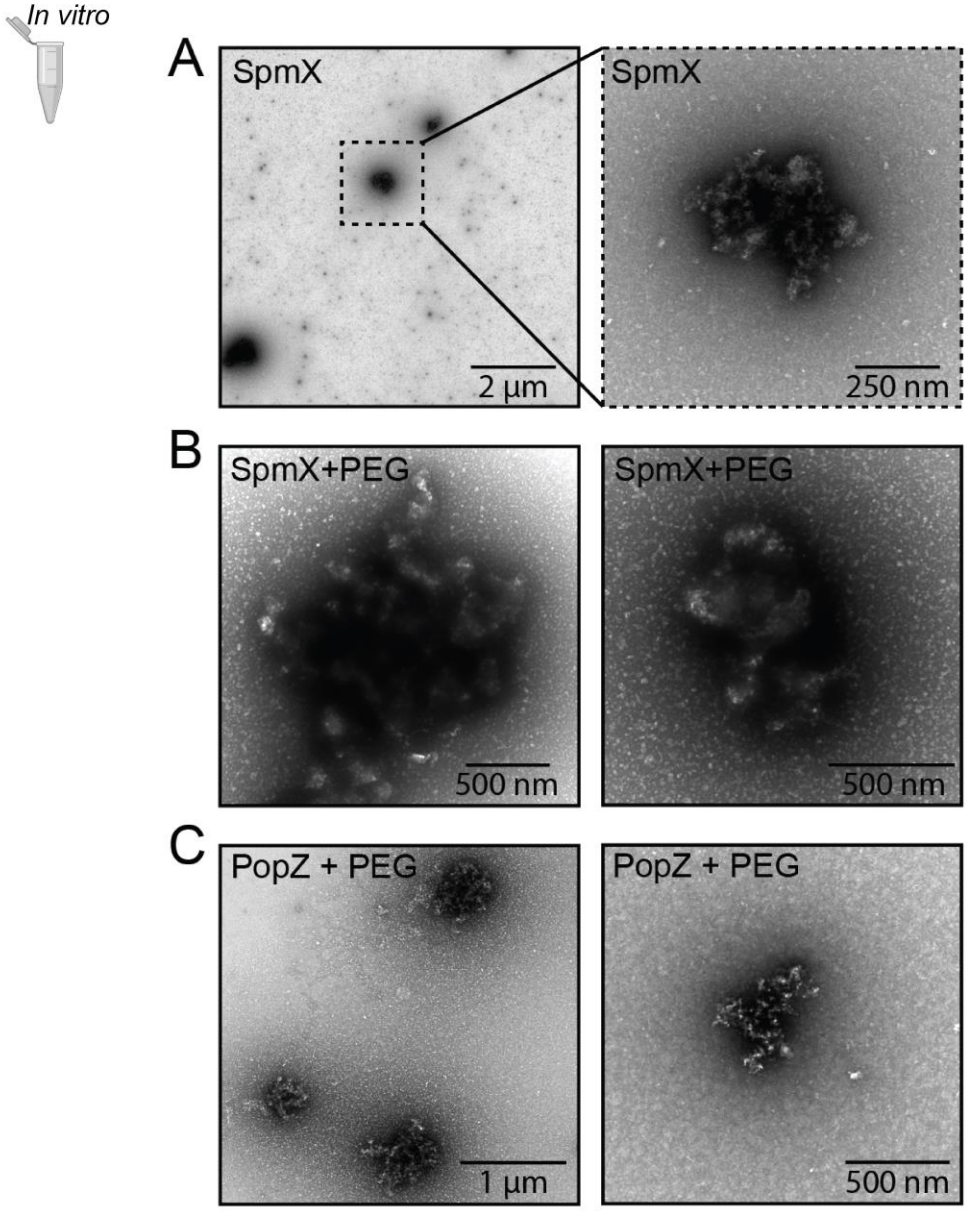

Figure S1. *Electron microscopy of PopZ and SpmX condensates*. A. 500nM SpmX (ΔTM) incubated for 2 hours at room temperature followed by negative staining using Uranyl acetate and imaging on a transmission EM. B. 500nM SpmX (ΔTM) incubated in a buffer (50 mM Hepes-KOH, pH 7.2) containing 100mg/mL PEG-6k for 2 hours at room temperature followed by negative staining using Uranyl acetate and imaging on a transmission EM. C. 500nM PopZ incubated for 2 hours at room temperature in a buffer containing 10mg/mL PEG-6k followed by negative staining using Uranyl acetate and imaging on a transmission EM.

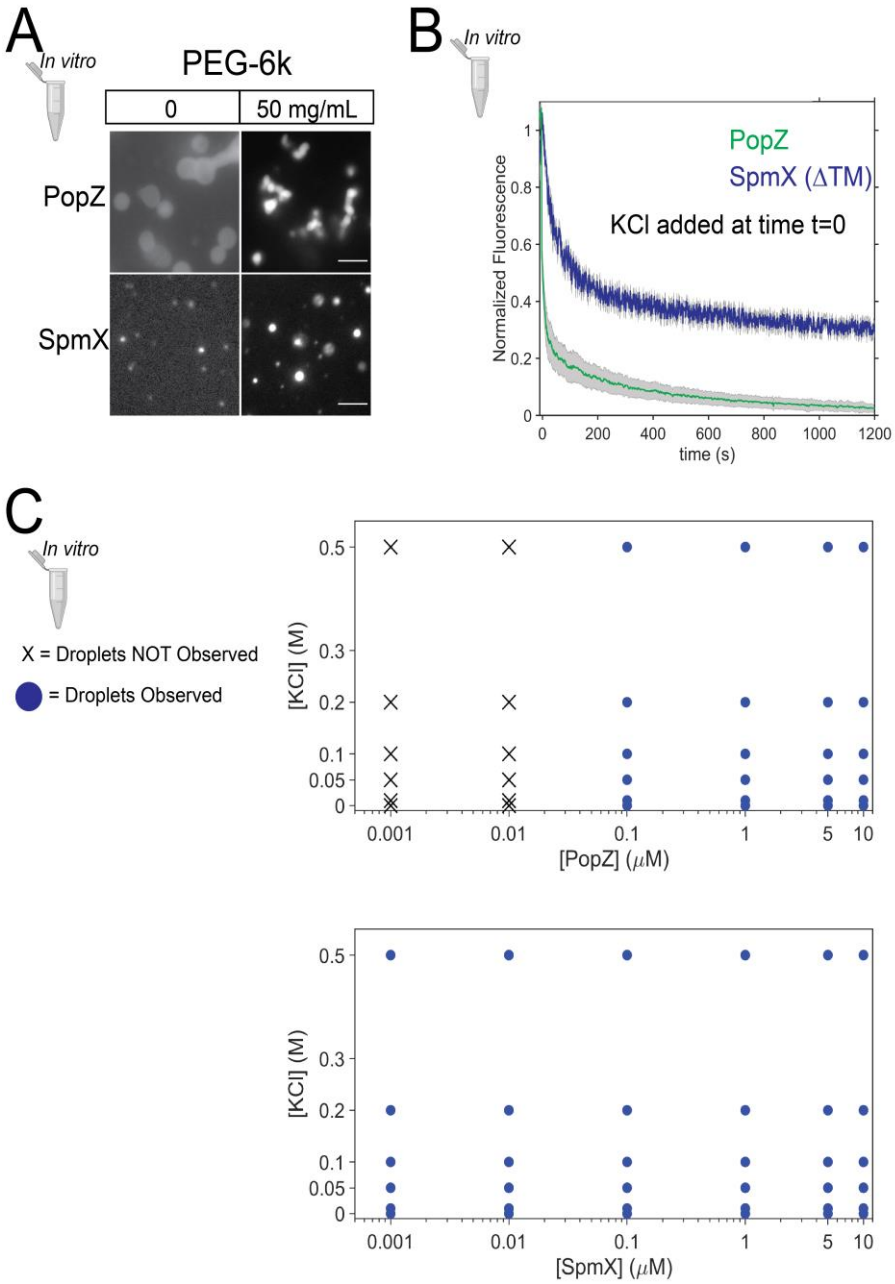

Figure S2. *Role of crowding and salt in condensate formation.* A. Crowding promotes phase separation. Fluorescence micrographs of PopZ (Atto488, 5μM) and SpmX (ΔTM, Cy3, 2μM) incubated in a buffer (50 mM Hepes-KOH, 0.1M KCl, pH 7.2) without (left column) or with (right column) PEG-6k for 5 hours. For a given protein, both images are scaled to the same brightness and contrast for comparison. B. Reversibility of PopZ and SpmX phase separation by addition of KCl. PopZ (Atto488) or SpmX (ΔTM, Cy3) were incubated at 5μM for 4 hours in KCl-free buffer (50 mM Hepes-KOH, pH 7.2) to form

condensates and imaged by fluorescence microscopy. At time t=0, KCl was added to the imaging chamber (0.5M final concentration) and time lapse images were acquired. Background subtracted fluorescence intensity (camera counts) from 20 condensates was measured for each time lapse experiment. Averaged data from all condensates was normalized to the intensity before KCl addition to obtain the curves shown. C. Phase diagram for purified PopZ (Atto488) (top) and SpmX (ΔTM, Cy3) (bottom) as a function of salt concentration. For each point, protein dialyzed against salt free buffer at a given concentration was incubated in a buffer containing the specified amount of potassium chloride (KCl) for 2 hours. The proteins were imaged on a widefield epi-fluorescence microscope with appropriate excitation and emission collection.

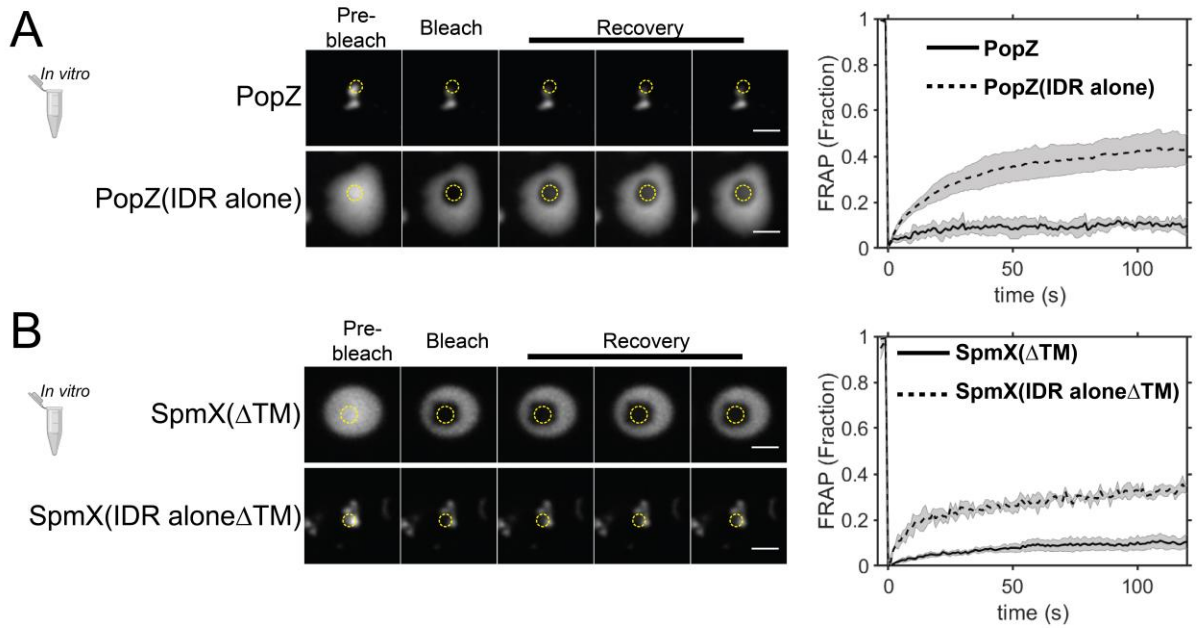

Figure S3. *Assessment of protein self-interaction within condensates by FRAP.* A. Confocal micrographs showing fluorescence recovery after photobleaching (FRAP) measurements of 2µM PopZ (top panel) or 2µM PopZ (aa 1-102) (lower panel). PopZ is labeled with Atto488. The recovery frames are from 20, 60 and 100 seconds, respectively. B. FRAP measurements for 2µM SpmX (aa 1-355, Cy3, top panel) or 2µM SpmX (AA156-355 N-terminal eYFP fusion, bottom panel). The recovery frames are from 20, 60 and 100 seconds, respectively. Scale bars are 2µm. Proteins were incubated in a buffer (50 mM Hepes-KOH, 0.1M KCl, pH 7.2) for 3 hours followed by FRAP on a spinning disk confocal microscope. Quantification of the average fluorescence intensity (normalized to the pre-bleach intensity and corrected for photobleaching) inside the bleached region across 5 individual protein condensates are shown below the fluorescence images. Error bars (gray area around the black curve) are standard error of the mean for the measurement.

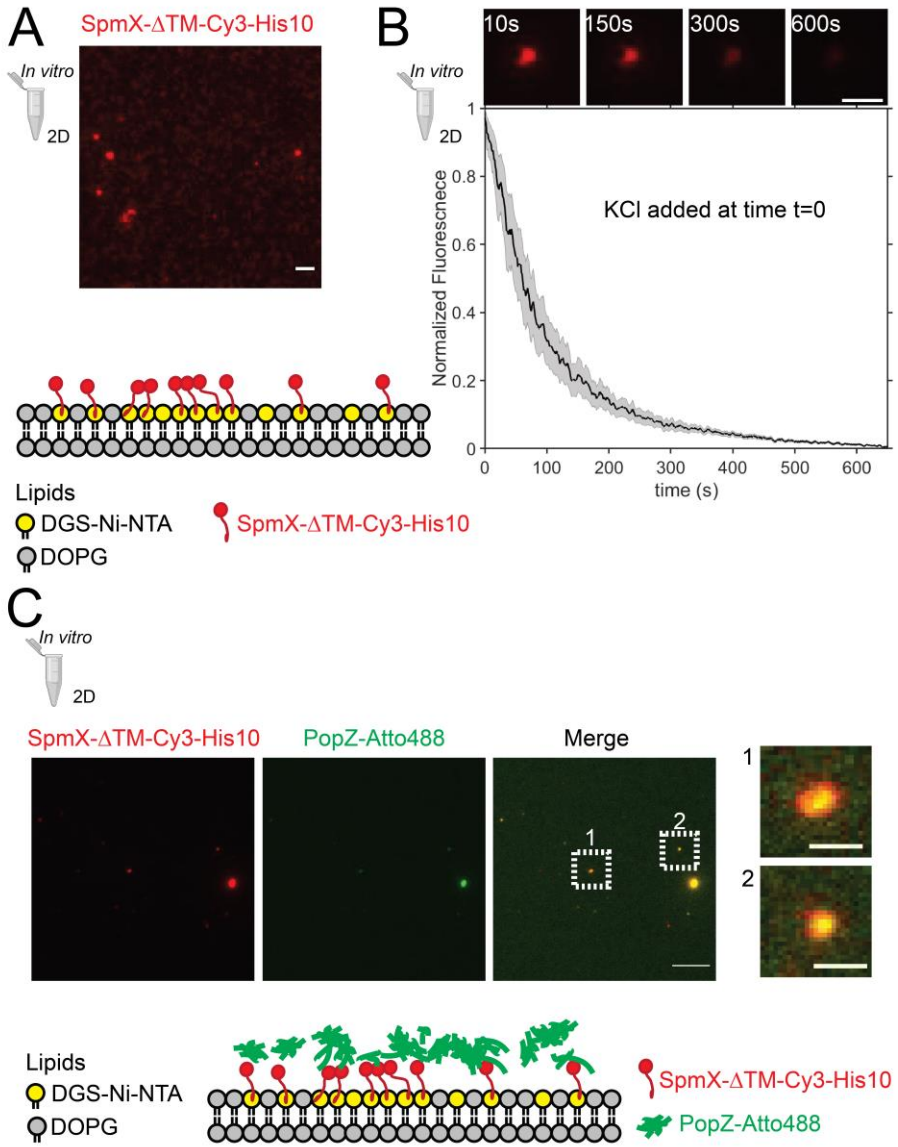

Figure S4. *SpmX phase separates and binds PopZ on a supported lipid bilayer*. A. (top) Representation of SpmXΔTM-Cy3-His-10 attached to DGS-Ni-NTA on the lipid bilayer. (bottom) SpmXΔTM-Cy3-His10 incubated at room temperature on a supported lipid bilayer (SLB) exhibits fluorescent puncta ranging in size from diffraction limited spots to 1 µm. Scale bar is 1µm. B. Time series of SpmXΔTM-Cy3-His 10 puncta on the SLB after the addition of 0.25M KCl. The addition of salt dissolves the puncta, as expected for phase separated condensates. Shown below the time series of the fluorescence images is a quantification of the average fluorescence intensity (background subtracted) across 10

individual protein condensates. Error bars (gray) are standard error of the mean of the measurements. C. PopZ and SpmX colocalize on SLBs. SpmXΔTM-Cy3-His10 was dispersed across an SLB and incubated for 2 hours followed by washing out the unbound proteins using 300 µL (10-flow cell volume) of clustering buffer (50 mM HEPES (pH 7.5), 150 mM KCl, 1 mM DTT, and 1 mg/mL BSA). PopZ-Atto488 was subsequently dispersed across the SLB containing the SpmX condensates and incubated for 2 hours followed by washing out the unbound proteins using 300 µL of clustering buffer. Fluorescence micrographs show two individual fluorescence channels and the merged channel with colocalization of SpmX-Cy3 and PopZ-Atto488 signal on the SLB. Scale bar shown in merged image is 2 µm. Regions 1 and 2 are representative condensates and are zoomed in for clarity. Scale bars are 1µm.

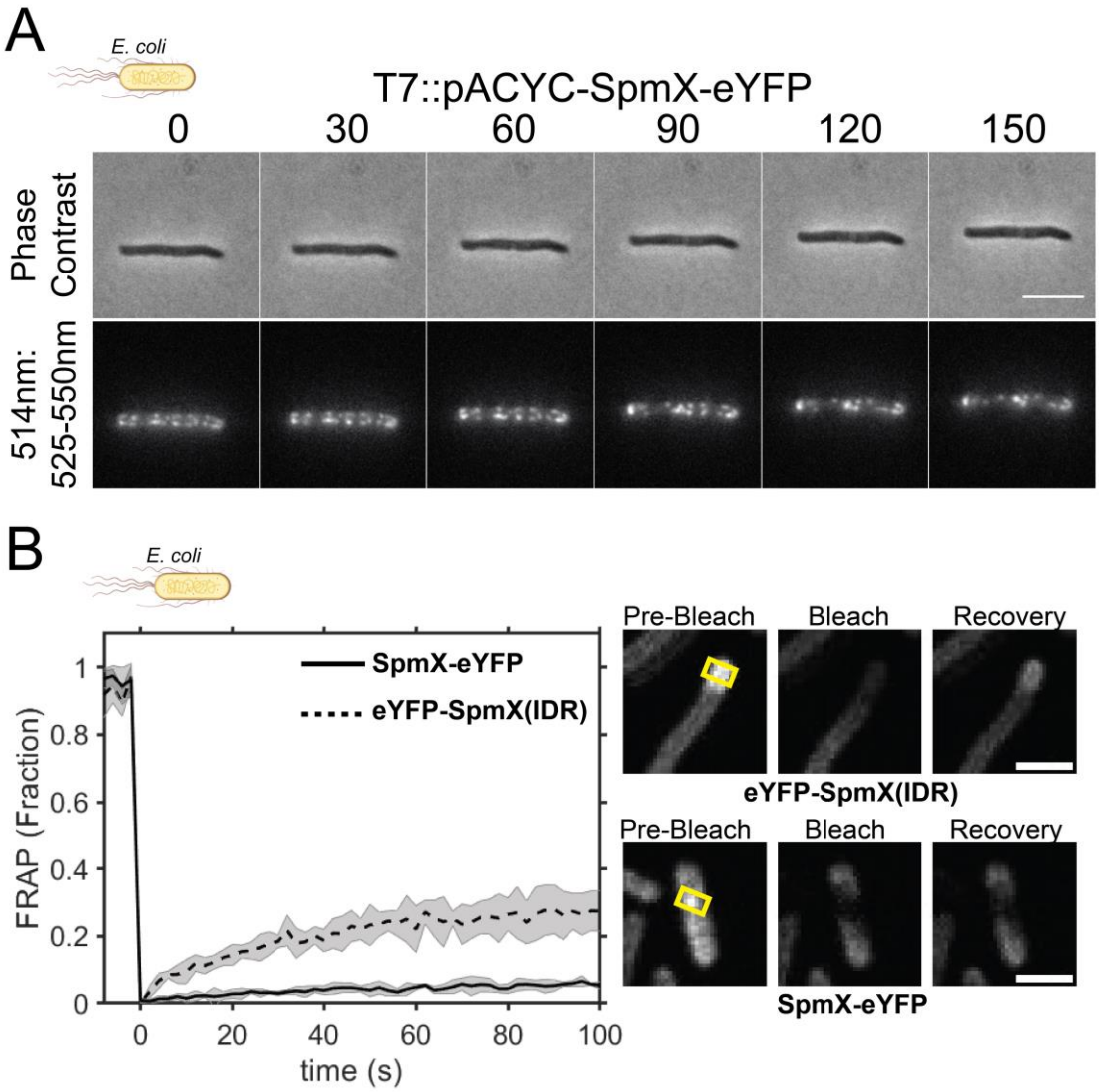

Figure S5. *SpmX phase separates in a living cell*. A. Wide-field Fluorescence micrograph of a time lapse showing phase separation of SpmX-eYFP expressed on a low copy pACYC plasmid in *E. coli* (BL21(DE3)) cells. Cells were induced with 100µM IPTG for 1 hour in M9G media (M9 supplemented with 0.4% Glucose) followed by washing using M9 media and resuspending in M9G media. 1µL of cells was spotted on agarose pads made in M9 media. The sample was excited using a LED source centered around 514 nm and fluorescence was collected from 525-550 nm. As time progressed (time in minutes shown above images), the membrane bound signal becomes more punctate, getting enriched at the cell poles and mid-cell region. Also see SI video 6. Scale bar is 5µm. B. FRAP performed on confocal microscope for WT SpmX-eYFP and eYFP-SpmX-IDR (AA156-431) alone show that the IDR has a higher recovery compared to the WT SpmX in *E. coli*.

FRAP curves are normalized to the pre-bleach intensity and corrected for photobleaching inside the bleached region across 4 individual cells. Error bars (gray area around the black curve) denote the standard error of the mean. These measurements support the *in vitro* results shown in Figure S4B. Scale bar is 2µm

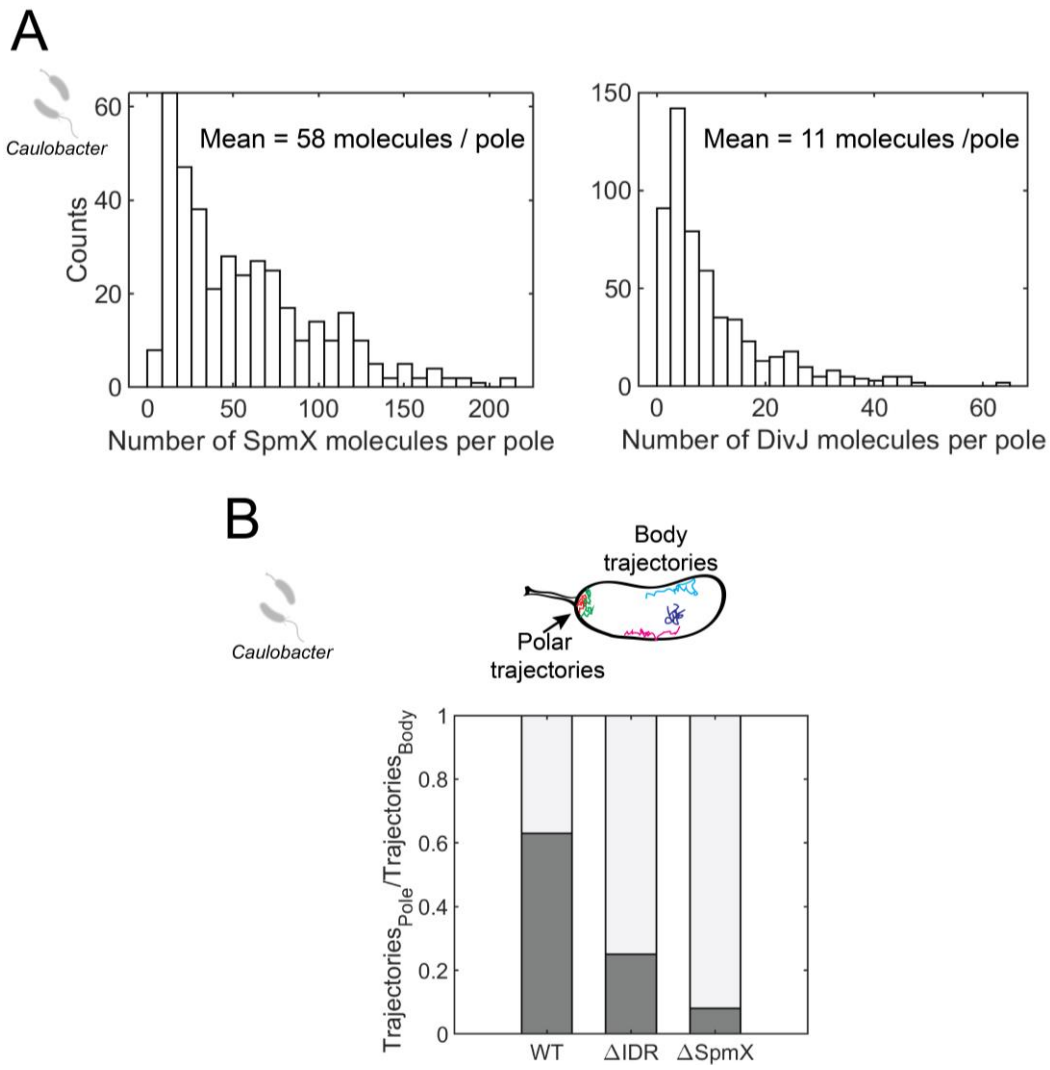

Figure S6. *Protein numbers and polar localization as measured by single molecule imaging.* A. Distribution of the number of SpmX molecules and DivJ molecules observed at the pole in a mixed population of *Caulobacter crescentus*. These distributions were obtained from wide-field fluorescence images. Samples were imaged continuously until the fluorescence signal bleached down to single molecule level. The intensity at the pole in the first diffraction limited image is divided by the mean intensity from a distribution of single eYFP molecules at the same laser power. A 31% correction based on the cell doubling time and eYFP maturation time was applied to account for immature eYFP species. B. Fraction of single molecule DivJ trajectories observed in the pole vs the body for respective strains. Total tracks analyzed are 1558 (WT), 1764 (SpmXΔIDR) and 3572 (ΔSpmX). DivJ is endogenously tagged using Halo enzyme and labelled with JF549-HaloTag dye.

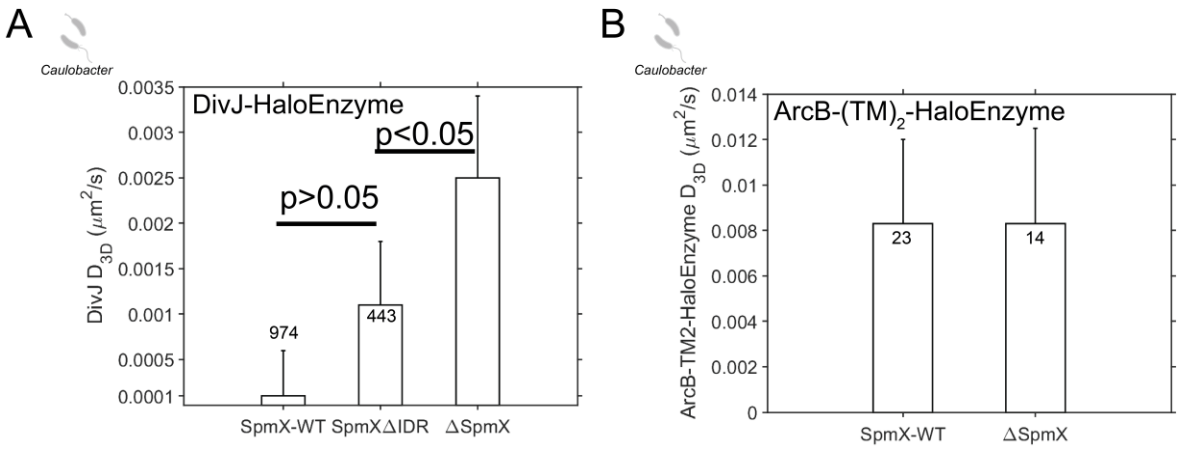

Figure S7. *Single molecule diffusion analyses using MSD for DivJ and a control protein.* (A) Three-dimensional diffusion coefficients obtained from Mean Squared Displacement (MSD) analyses for polar DivJ trajectories in various SpmX backgrounds. The number of trajectories analyzed for each sample are noted with the bars. P values from a pairwise two-tailed t-test are denoted in the plot. (B) 3D diffusion coefficients obtained from MSD analyses of control trans-membrane Halo enzyme trajectories in WT and SpmX deletion backgrounds. The Halo enzyme is attached to the membrane using two trans-membrane helices from the *E. coli* protein ArcB. These domains have no homology with any *Caulobacter* proteins and thus the Halo enzyme fusion serves as an inert control. Differences were not detected in the diffusion coefficients of the Halo enzyme in WT or SpmX deletion backgrounds. Errors in D in both panels (A) and (B) are standard deviations estimated from bootstrapping (50% sampling with replacement performed 500 times).

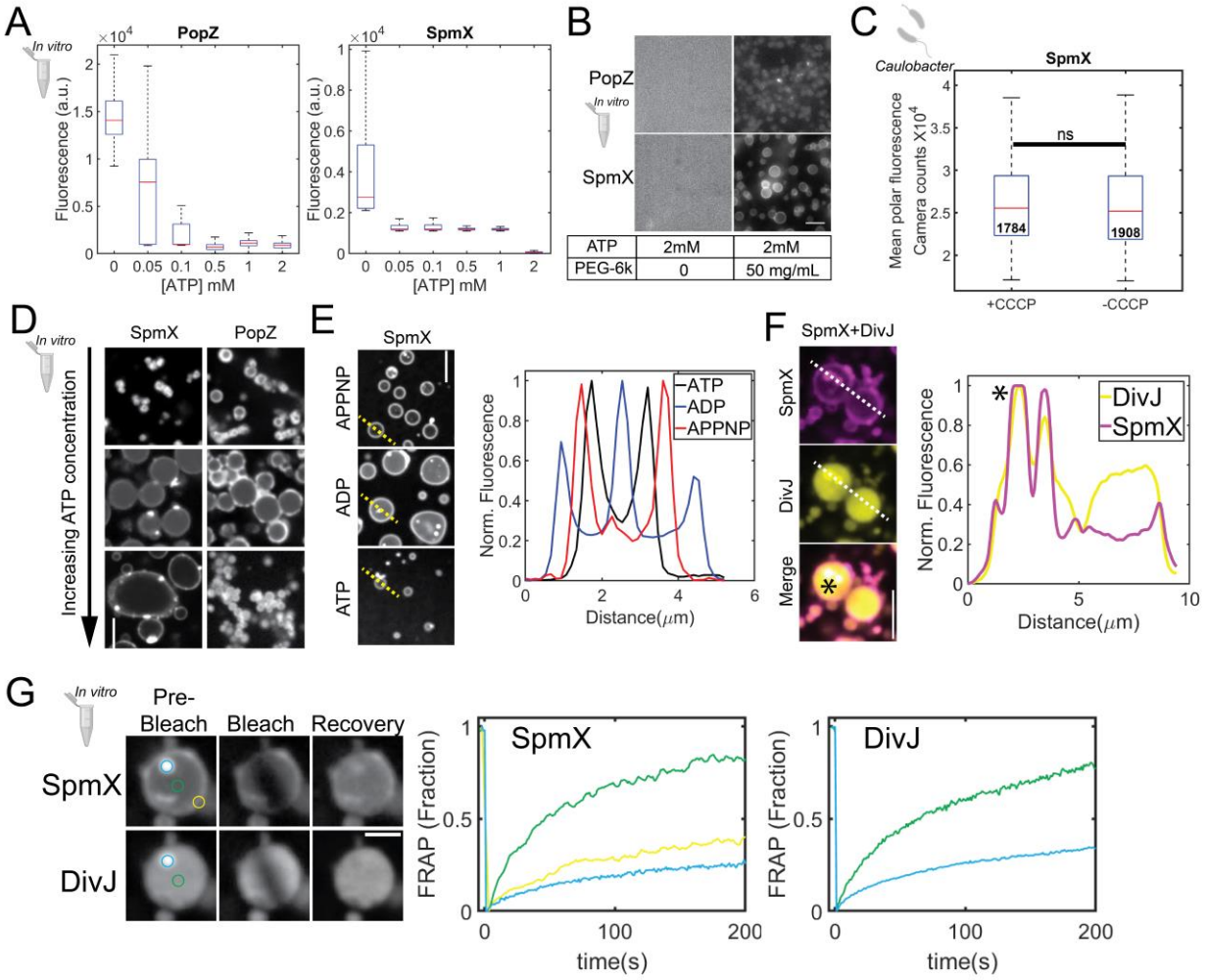

Figure S8. *Characterization of ATP's hydrotrope effect on PopZ and SpmX condensates*. A. Quantification of the average intensity of observed condensates of fluorescently-labeled PopZ (Atto488) and SpmX (ΔTM, Cy3) titrated against ATP concentrations ranging from 0 to 2mM. ATP was added to 5μM protein sample at indicated concentrations and the sample was imaged after incubating at room temperature for 2 hours (image data in Fig. 3A). Red lines within the boxes denote the median fluorescence intensity values and the capped-dotted lines denote the maximum and minimum values of fluorescence intensities. B. Fluorescence micrographs showing that addition of the crowding agent PEG-6k opposes dissolution by ATP for both PopZ and SpmX(ΔTM). Protein samples at 5μM concentration were incubated in buffer (50 mM HEPES-KOH pH 7.4, 100 mM KCl) either with or without 50mg/mL PEG-6k for 8 hours followed by addition of 2mM ATP and incubation for 2 hours. C. Box plot showing average polar fluorescence

signal from cells expressing SpmX-eYFP as the sole protein copy in *Caulobacter* cells. Cells were grown in M2G and split into two tubes, one treated with 100 µM CCCP in DMSO and the other treated with an equivalent volume of DMSO for 10 mins. Red lines denote the median values and N is the number of cells analyzed to obtain the data. NS – not significant based on a two-sample t-test at 95% confidence interval. D. Observation of protein bubbles with PopZ (Atto488) incubated with 0.1, 0.5 and 1 mM ATP for 30 minutes (top) and SpmX (ΔTM, Cy3) incubated with 0.5, 1 and 2mM ATP for 30 minutes (bottom). Also see SI video 7. E. Confocal fluorescence micrographs of SpmX (ΔTM, Cy3 labeled) bubbles were observed by incubating the protein with 1mM ATP, ADP or APPNP. Adjacent image shows the line profile of the bubbles at the dashed lines drawn for each image. F. Multicolor confocal micrographs of SpmX (ΔTM, Cy3) and DivJ (ΔTM, Atto488) complexed in the presence of 1mM ATP. DivJ-Atto488 signal is not enriched at the bubble boundary but is enriched in SpmX condensates within the bubble denoted by the Asterisk. G. (Left) Confocal fluorescence micrographs for SpmX (ΔTM, Cy3) and DivJ (ΔTM, Atto488) in a complex at a concentration of 5µM each. (Right) FRAP curves for the regions marked in the left panel showing the presence of a highly mobile phase, an intermediate phase, and a low mobility condensate phase inside the protein bubble. A representative FRAP curve is shown as these bubbles were dynamic and replicates in the same sample could not be measured. For all images in this figure scale bar is 5µm.

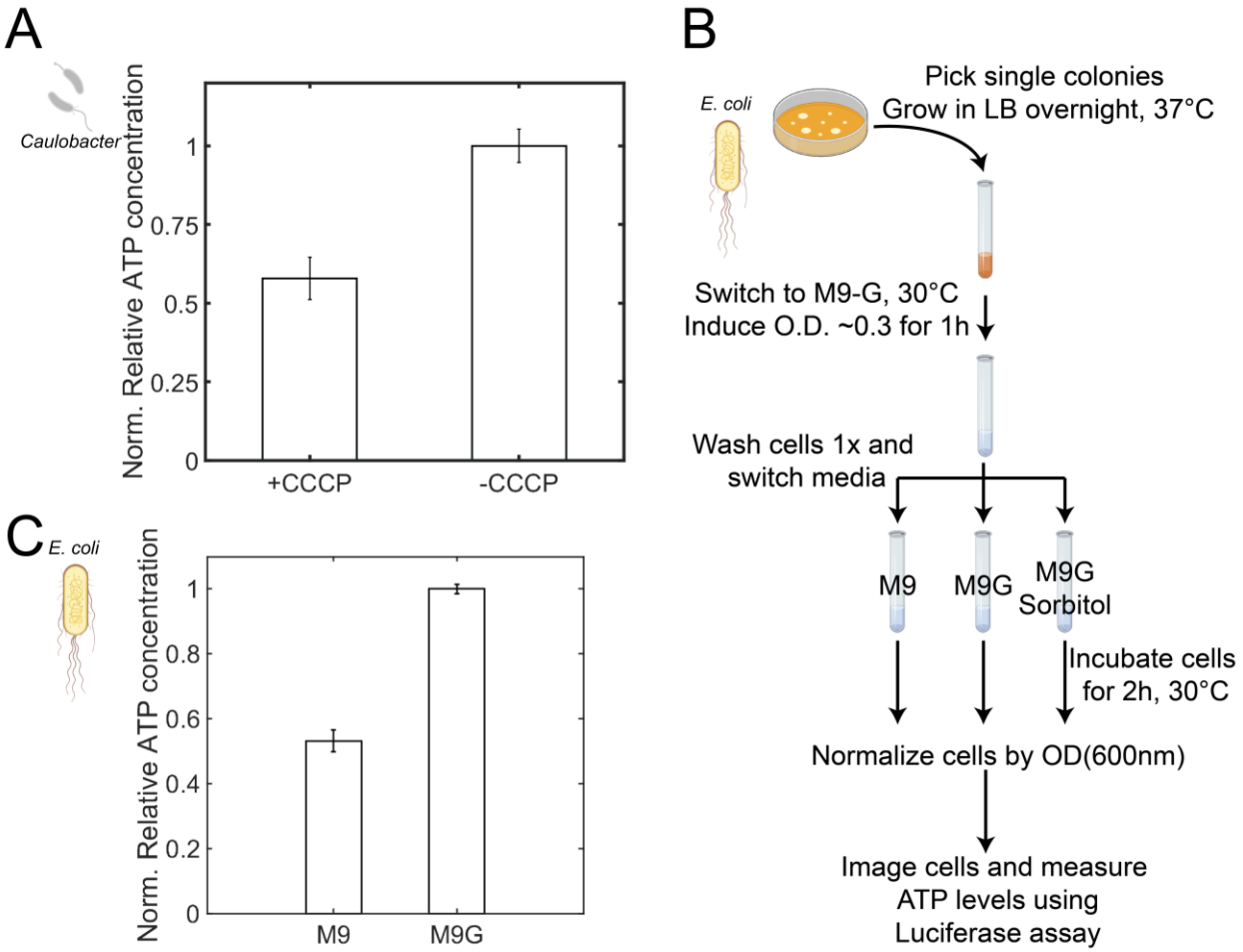

Figure S9. *ATP measurements in Caulobacter and E. coli.* A. Relative intracellular ATP concentrations from cells treated with CCCP or DMSO. Measurements were performed using a commercial Luciferase based assay. Relative luminescence units were background subtracted and the data were normalized to the ATP levels in the DMSO case. Error bars represent the standard deviations from 3 biological replicates, with each sample assayed in triplicate. B. Schematic of the protocol used to measure intracellular ATP in *E. coli* (BL21(DE3)) cells grown in different minimal media: M9 minimal media without glucose, M9 minimal media supplemented with 0.4% glucose (M9G) and M9G supplemented with 0.5M Sorbitol (M9GS). C. Relative intracellular ATP concentrations from measurements performed using a Luciferase based assay. Relative luminescence units were background subtracted and the data were normalized to the ATP levels in M9G. Error bars are the standard errors of the mean from three biological replicates, each assayed in triplicate.

Files – Supplementary information

1. SI video 1: Video showing the reversibility of PopZ condensates *in vitro*. PopZ was fluorescently tagged using Atto488-NHS dye and 5µM protein was incubated in buffer (50 mM Hepes-KOH, 0.01M KCl, pH 7.2) at room temperature for 2 hours. The resulting solution was added to imaging chambers and a time lapse movie was recorded with 1 s interval between frames. At about 1 minute, 0.5M KCl was added to the imaging chambers carefully and time lapse imaging was continued for another 4 minutes.
2. SI video 2: Video showing the reversibility of SpmX condensates *in vitro*. SpmX was fluorescently tagged using an unnatural amino acid (p-Azido-N-phenylalanine substitution at position 338) and DBCO-Cy3 dye. 5µM of the protein was incubated in buffer (50 mM Hepes-KOH, 0.01M KCl, pH 7.2) at room temperature for 2 hours. The resulting solution was added to imaging chambers and a time lapse movie was recorded with 1 s interval between frames. At about 30 seconds, 0.5M KCl was added to the imaging chambers carefully and time lapse imaging was continued for another 24 minutes.
3. SI video 3: Maturation of PopZ condensates assembled as in SI video 1 but with 0.1M KCl in the buffer. The video was recorded for 3.5 hours and it is sped up by 250-times.
4. SI video 4: Maturation of SpmX (ΔTM, Cy3) condensates assembled as in SI video 2 but with 0.1M KCl in the buffer. The video was recorded for 3.8 hours and it is sped up by 260-times.
5. SI video 5: Video showing the reversibility of SpmX (ΔTM, Cy3) condensates *in vitro* on a supported lipid bilayer. Lipid bilayer assembly and protein incubation details are outlined in methods. 0.5M KCl was added to the flow-cell containing assembled SpmX-Cy3 condensates at about a minute in the video. Time lapse imaging was continued for another 10 minutes. The video is sped up 10-times.
6. SI video 6: Time lapse video of an *E. coli* cell expressing SpmX-eYFP under the control of a T7 promoter. Cells were induced with 100µM IPTG for 1 hour in M9G media (M9 supplemented with 0.4% Glucose) followed by washing using M9 media

and resuspending in M9G media. 1µL of cells was spotted on agarose pads made in M9 media. Images were acquired every 15 minutes. Also see Fig. S5A.

7. SI video 7: Observation of dynamic bubble-like condensates of SpmX (ΔTM, Cy3) incubated in the presence of ATP. 5µM of the protein was incubated in buffer (50 mM Hepes-KOH, 0.1M KCl, pH 7.2) at room temperature for 2 hours. 2mM ATP was added to the sample followed by incubation at room temperature for 30 minutes. Images were captured every 10 seconds and the movie was recorded for about 25 minutes. The jitter in the bubbles is likely due to bubble fusion events along the z-axis (into the plane of the image).
8. Materials and methods

References

1. S. Boeynaems *et al.*, Protein phase separation: A new phase in cell biology. *Trends in Cell Biology.* **28**, 420-435 (2018).

2. P. Li *et al.*, Phase transitions in the assembly of multivalent signalling proteins. *Nature.* **483**, 336-340 (2012).

3. E. Hock *et al.*, Hypertonic stress causes cytoplasmic translocation of neuronal, but not astrocytic, FUS due to impaired transportin function. *Cell Reports.* **24**, 987-1000.e7 (2018).

4. K. Simpson-Lavy, T. Xu, M. Johnston, M. Kupiec, The Std1 activator of the Snf1/AMPK kinase controls glucose response in yeast by a regulated protein aggregation. *Molecular Cell.* **68**, 1120-1133.e3 (2017).

5. J. A. Theriot, Why are bacteria different from eukaryotes? *BMC Biology.* **11**, 119 (2013).

6. N. Al-Husini, D. T. Tomares, O. Bitar, W. S. Childers, J. M. Schrader, α-Proteobacterial RNA degradosomes assemble liquid-liquid phase-separated RNP bodies. *Molecular Cell.* **71**, 1027-1039.e14 (2018).

7. B. Monterroso *et al.*, Bacterial FtsZ protein forms phase-separated condensates with its nucleoid-associated inhibitor SlmA. *EMBO Reports.* **20**, n/a (2019).

8. F. Heinkel *et al.*, Phase separation and clustering of an ABC transporter in Mycobacterium tuberculosis. *Proceedings of the National Academy of Sciences - PNAS.* **116**, 16326-16331 (2019).

9. A. Ladouceur *et al.*, Clusters of bacterial RNA polymerase are biomolecular condensates that assemble through liquid–liquid phase separation. *Proceedings of the National Academy of Sciences - PNAS.*, 202005019 (2020).

10. K. Lasker *et al.*, Selective sequestration of signalling proteins in a membraneless organelle reinforces the spatial regulation of asymmetry in *Caulobacter crescentus*. *Nature Microbiology.* **5**, 418-429 (2020).

11. M. Feric *et al.*, Coexisting Liquid Phases Underlie Nucleolar Subcompartments. *Cell.* **165**, 1686-1697 (2016).

12. Y. Shin, C. P. Brangwynne, Liquid phase condensation in cell physiology and disease. *Science (New York, N.Y.).* **357**, eaaf4382 (2017).

13. L. Shapiro, H. H. McAdams, R. Losick, Why and how bacteria localize proteins. *Science.* **326**, 1225-1228 (2009).

14. G. R. Bowman *et al.*, Oligomerization and higher-order assembly contribute to sub-cellular localization of a bacterial scaffold. *Molecular Microbiology.* **90**, 776-795 (2013).

15. S. K. Radhakrishnan, M. Thanbichler, P. H. Viollier, The dynamic interplay between a cell fate determinant and a lysozyme homolog drives the asymmetric division cycle of *Caulobacter crescentus*. *Genes & Development.* **22**, 212-225 (2008).

16. A. M. Perez *et al.*, A localized complex of two protein oligomers controls the orientation of cell polarity. *mBio.* **8**, 2238 (2017).

17. A. Gahlmann *et al.*, Quantitative multicolor subdiffraction imaging of bacterial protein ultrastructures in three dimensions. *Nano Letters.* **13**, 987-993 (2013).

18. P. D. Dahlberg *et al.*, Cryogenic single-molecule fluorescence annotations for electron tomography reveal in situ organization of key proteins in *Caulobacter*. *Proc. Natl. Acad. Sci. USA.*, 202001849 (2020).

19. Deanne L. Pierce *et al.*, Mutations in DivL and CckA rescue a divJ null mutant of *Caulobacter crescentus* by reducing the activity of CtrA. *Journal of Bacteriology.* **188**, 2473-2482 (2006).

20. C. Tsokos, B. Perchuk, M. Laub, A dynamic complex of signaling proteins uses polar localization to regulate cell-fate asymmetry in *Caulobacter crescentus*. *Developmental Cell.* **20**, 329-341 (2011).

21. S. Alberti, A. Gladfelter, T. Mittag, Considerations and challenges in studying liquid-liquid phase separation and biomolecular condensates. *Cell.* **176**, 419-434 (2019).

22. X. Su *et al.*, Phase separation of signaling molecules promotes T cell receptor signal transduction. *Science (New York, N.Y.).* **352**, 595-599 (2016).

23. Yuichi Taniguchi *et al.*, Quantifying *E. coli* proteome and transcriptome with single-molecule sensitivity in single cells. *Science.* **329**, 533-538 (2010).

24. S. Bakshi, A. Siryaporn, M. Goulian, J. C. Weisshaar, Superresolution imaging of ribosomes and RNA polymerase in live Escherichia coli cells. *Molecular Microbiology.* **85**, 21-38 (2012).

25. J. B. Grimm *et al.*, A general method to improve fluorophores for live-cell and single-molecule microscopy. *Nature Methods.* **12**, 244-250 (2015).

26. L. Weimann *et al.*, A quantitative comparison of single-dye tracking analysis tools using Monte Carlo simulations. *PloS One.* **8**, e64287 (2013).

27. H. Lu *et al.*, Phase-separation mechanism for C-terminal hyperphosphorylation of RNA polymerase II. *Nature.* **558**, 318-323 (2018).

28. A. Klosin *et al.*, Phase separation provides a mechanism to reduce noise in cells. *Science (New York, N.Y.).* **367**, 464-468 (2020).

29. B. Parry *et al.*, The Bacterial cytoplasm has glass-like properties and is fluidized by metabolic activity. *Cell.* **156**, 183-194 (2014).

30. Stephanie C. Weber, Andrew J. Spakowitz, Julie A. Theriot, Nonthermal ATP-dependent fluctuations contribute to the in vivo motion of chromosomal loci. *Proceedings of the National Academy of Sciences of the United States of America.* **109**, 7338-7343 (2012).

31. A. Patel *et al.*, ATP as a biological hydrotrope. *Science (New York, N.Y.).* **356**, 753-756 (2017).

32. H. Yaginuma *et al.*, Diversity in ATP concentrations in a single bacterial cell population revealed by quantitative single-cell imaging. *Scientific Reports.* **4**, 6522 (2014).

33. N. Farhat, F. Hammes, E. Prest, J. Vrouwenvelder, A uniform bacterial growth potential assay for different water types. *Water Research.* **142**, 227-235 (2018).

34. B. Liu, Z. Hasrat, B. Poolman, A. J. Boersma, Decreased effective macromolecular crowding in Escherichia coli adapted to hyperosmotic stress. *Journal of Bacteriology.* **201**, 1 (2019).

35. L. J. Wu *et al.*, Localisation of DivIVA by targeting to negatively curved membranes. *The EMBO Journal.* **28**, 2272-2282 (2015).

36. Y. Lin, S. Crosson, N. F. Scherer, Single-gene tuning of *Caulobacter* cell cycle period and noise, swarming motility, and surface adhesion. *Molecular Systems Biology.* **6**, 445-n/a (2010).

37. D. B. Roszak, R. R. Colwell, Survival strategies of bacteria in the natural environment. *Microbiological Reviews.* **51**, 365-379 (1987).

38. M. Y. Lobanov, O. V. Galzitskaya, How common is disorder? Occurrence of disordered residues in four domains of life. *International Journal of Molecular Sciences.* **16**, 19490-19507 (2015).

39. Z. Dosztányi, V. Csizmok, P. Tompa, I. Simon, IUPred: web server for the prediction of intrinsically unstructured regions of proteins based on estimated energy content. *Bioinformatics (Oxford, England).* **21**, 3433-3434 (2005).

40. E. S. Freeman Rosenzweig *et al.*, The eukaryotic CO2-concentrating organelle is liquid-like and exhibits dynamic reorganization. *Cell.* **171**, 148-162.e19 (2017).

41. S. Saurabh, A. M. Perez, C. J. Comerci, L. Shapiro, W. E. Moerner, Super-resolution Imaging of Live Bacteria Cells Using a Genetically Directed, Highly Photostable Fluoromodule. *Journal of the American Chemical Society.* **138**, 10398-10401 (2016).

42. I Contreras, L Shapiro, S Henry, Membrane phospholipid composition of *Caulobacter crescentus*. *Journal of Bacteriology.* **135**, 1130-1136 (1978).

43. T. H. Mann, W. Seth Childers, J. A. Blair, M. R. Eckart, L. Shapiro, A cell cycle kinase with tandem sensory PAS domains integrates cell fate cues. *Nature Communications.* **7**, 11454 (2016).

44. A. Ertel, A. G. Marangoni, J. Marsh, F. R. Hallett, J. M. Wood, Mechanical properties of vesicles. I. Coordinated analysis of osmotic swelling and lysis. *Biophysical Journal.* **64**, 426-434 (1993).

45. J. Pan *et al.*, Molecular structures of fluid phase phosphatidylglycerol bilayers as determined by small angle neutron and X-ray scattering. *BBA - Biomembranes.* **1818**, 2135-2148 (2012).